TAMPEREEN TEKNILLINEN YLIOPISTO
TAMPERE UNIVERSITY OF TECHNOLOGY

ELIAS YIMAM

FABRICATION OF VANADIUM OXIDE NANOPARTICLES BY PULSED LASER ABLATION

Master of Science Thesis

Examiner: Professor Tapio Niemi
Adviser: Turkka Salminen (Dr.)
Examiner and topic approved by the Council of the Faculty of Natural Sciences on 14 August 2013

ABSTRACT

TAMPERE UNIVERSITY OF TECHNOLOGY
Master's Degree Programme in Science and Bioengineering
Elias, Yimam: Fabrication of Vanadium Oxide Nanoparticles by Pulsed Laser Ablation
Master of Science Thesis, 62 pages, 1 Appendix page
August 27th 2014
Major: Nanotechnology
Examiner: Professor Tapio Niemi
Keywords: Pulsed laser ablation in liquid, vanadium oxides, vanadium dioxide, vanadium pentoxide

Pulsed laser ablation in liquid (PLAL) is an eco-friendly nanoparticles fabrication technique. PLAL uses laser light to ablate a solid material which is submerged in a liquid medium. During the interaction of laser light with the solid target plasma will be formed. In the high pressure and temperature of the plasma, nanoparticles are formed.

This thesis deals with PLAL for synthesis of vanadium oxide. Vanadium oxide refers to an inorganic compound with general formula of V_nO_{2n+1}. There are approximately 15-20 stable vanadium oxides. Out of these, eight oxides show reversible phase transition from a semi-conducting phase to a metallic phase at a critical temperature (T_c). The range of temperatures where the transition occurs is between -147℃ to 375℃. The T_c for most commonly used vanadium oxides are 68 ℃ (VO_2), -105 ℃ (V_2O_3) and +375 ℃ (V_2O_5).

The phase transition is accompanied by a change in crystal structure, optical and electrical properties. These temperature dependent changes have applications in optics and electronics.

The aim of the thesis is to investigate possible methods to synthesis vanadium oxides by PLAL. Fabrication of less thermodynamically stable oxides (such as VO_2, V_2O_3) demands careful control of the process parameters. Special attention is devoted for fabrication of VO_2 because of its T_c is near to room temperature. It can be used for window coatings, opto-electronic memories, and switches.

In the experiments, pure vanadium (99.8%) metal-target is ablated by a high repetition rate fiber laser in a liquid medium. The liquid has a significant influence on the reactivity and stability of the particles and great care was taken in the selection of liquid during the experiments. Different liquids such as acetone, ethanol, methanol, water, pyridine, acetonitrile, stabilizer Sodium Dodecyl Sulfate (SDS) and as oxidizing agent hydrogen peroxide are used.

This thesis work has produced $V_2O_5.nH_2O$ gel and it was converted to VO_2 by annealing in vacuum chamber. Fibers like nanoparticles of VO_X were synthesized by PLAL in acetone-water mixture and acetonitrile-acidified water mixtures. Pure vanadium nanoparticles were produced in polar aprotic solvents (acetone, pyridine and acetonitrile). The synthesized products were characterized by Scanning Electron Microscopy (SEM), Transmission Electron Microscopy (TEM), Optical Spectroscopy and Raman Spectrometry.

PREFACE

This thesis was done between May 5th 2013 and August 27th 2014 at the Optoelectronics Research Center (ORC) in the nanophotonics research group. The nanophotonics research group is led by Prof. Tapio Niemi. Fabrication of nanoparticles by pulsed laser ablation in liquids is one of the research areas in which Dr. Turkka Salminen and Prof.Tapio Niemi are working.

First of all, I would like to express my gratitude to Prof. Tapio Niemi for his permission to carry out my thesis at ORC. I am so grateful for the time I spent under his supervision and I would like to thank him for his encouraging support. During my thesis work he was cooperative in providing the necessary materials and moral support.

I would like to thank Dr. Turkka Salminen for his guidance and day to day support. Without his dedicative assistance this thesis would not have been possible. He has devoted his valuable time to train me on handling the experiment, characterizing the products by Raman spectroscopy and scanning electron microscopy. He has forwarded valuable comments to improve the thesis during the experiment and in the writing process.

I would like to thank Dr. Mari Honkanen and Mr. Erkka Frankberg from the department of materials science. Dr. Mari Honkanen has provided assistance in characterizing the sample with TEM and EDX. Mr. Erkka Frankberg has provided assistance in annealing vanadium samples in a vacuum chamber for production of VO_2. Last but not least, I would like to forward my special thanks to my family and friends for their unconditional love and support. I would like to forward my special gratitude to my older brother Fikru who is responsible for laying the foundation of my academic career at a very young age and inspiring me to carry on my education further to the highest level. I would like to express my special respect and affection to my mother and father (Ethanesh and Zewdu)

Tampere, September 2014

Elias Zewdu Yimam
ኤልያስ ዘዉዱ ይማም
eliaszewdu@yahoo.com

TABLE OF CONTENTS

LIST OF SYMBOLS AND ABBREVIATIONS

Abbreviations

ATM	Atmospheric pressure
CCD	Charge coupled device
DC	Direct current
DI-water	De ionized water
EPD	Electrophoretic deposition
LCD	Liquid crystal display
LDS	Lithium dodecyl sulfate
Nd:YAG	Neodymium-doped yttrium aluminium garnet
PLAL	Pulsed laser ablation in liquid
PMT	Photomultipliers
SDS	Sodium dodecyl sulfate
SE	Secondary electrons
SEM	Scanning electron microscope
T_c	Critical temperature
TEM	Scanning electron microscope
T_i	Lattice heating time
T_L	Laser pulse duration

Symbols, Greek alphabet

ε	Permittivity
ζ	Zeta potential
η	Viscosity
λ	Wavelength
μ	Carrier mobility
ρ	Density
σ	Conductivity
σ_o	Conductivity
	Pre-exponential factor

Symbols, elements and compounds

A	Absorption
a	Electrode surface area
Ag	Silver
Al	Aluminum
Ar	Argon
c	The heat capacity
C	Particles concentration
Ca	Calcium
CdS	Cadmium sulfide
Ce	Cerium
Cl	Chlorine
Co	Cobalt
CO	Carbon monoxide
Cr	Chromium
Cu	Copper
E	Strength of an electric field
E_a	Activation energy
E_c	Lowest energy of the conduction band
E_f	Energy of the Fermi level
F	Fluence
Fe	Iron
G	Total free energy
Ga	Gallium
Ge	Germanium
G_{metal}	The total free energy of the metal
G_{smi}	The total free energy of the semiconductor
H	The enthalpy
h	Heat diffusion length
H_2	Hydrogen molecule
H_2O_2	Hydrogen peroxide
I	Transmitted light
In	Indium
I_O	Incident light
K	Boltzmann constant
l	length of electrode
m	Deposited mass
Mo	Molybdenum
Mg	Magnesium
Mn	Manganese
n	Electron concentration
N_2	Nitrogen gas
NaOH	Sodium hydroxide
Nb	Niobium
N_c	Effective density
NH_3	Ammonia
P	Phosphorus

Pb	Lead
pH	Measure of the acidity or basicity of a solution
q	Charge of electron
R	Reflectivity
r_1	Radius of the electrode 1
r_2	Radius of the electrode 2
S	The entropy
Si	Silicon
SnO_2	Tin dioxide
SO_2	Sulfur dioxide
SO_3	Sulfur trioxide
t	Deposition time
Ta	Tantalum
Ti	Titanium
TiO_2	Titanium dioxide
V	Vanadium
ΔV	Shift in frequency
Vm	De-excitation frequency
Vo	Incident beam frequency
VO	Vanadium monoxide
VO_2	Vanadium dioxide
V_2O_5	Vanadium pentoxide
V_2O_3	Vanadium trioxide
W	Tungsten
ZnO	Zinc monoxide
ZnSe	Zinc Selenide

INTRODUCTION

Functional metallic oxides have drawn the attention of numerous researchers, especially for designing of materials such as sensing, energy storage, optics and electronics [1]. Controlling functional metallic oxides dimensions (size and shape) at nanoscale allows tailoring of material properties. For instance, the band gap of semiconductor quantum dots depends on size. Nanoparticles within size range of 1-100 nm exhibit noticeable size dependent properties. Harnessing size dependent properties of material is the foundation of nanotechnology [2].

VO_2 is categorized as a functional metallic oxide. It exhibits a phase transition from the semiconductor to the metal phase at a critical temperature, which is approximately 68 ℃. The phase transition occurs because of the lattice structure changes. The structure of VO_2 at a temperature below the critical value is monoclinic exhibiting semiconductor properties and above the critical value, the structure transforms to Rutile crystal lattice which has metallic properties [3]. These structural changes are also observed as change in optical and electrical properties. Subsequently, these phenomena can be tailored and integrated to design various products and for applications such as, electrical or optical switch [4], optical storage [5], erasable optical data recording [6], and thermal sensors [7].

Various nanoforms of VO_2 (nanoparticles, nanobelts, nanowires) are produced by different mechanisms, for instance, from ammonium metavanadate precursor using hydrothermal method it is possible to synthesize metastable vanadium dioxide nanobelts [8]. Size controlled vanadium dioxide nanocrystals can be synthesized in a fused silica matrix using thermal annealing method [9]. Well faceted VO_2 nanowires with rectangular cross sections are synthesized by vapour transport method using VO_2 powder as precursor [10].

VO_2 thin film coatings can be achieved by various techniques, such as chemical vapour deposition, sol-gel synthesis, sputter deposition and pulsed laser deposition [11]. However, the conventional synthesis methods (mechanical milling and chemical) are economically expensive, technically complex, challenging to control size and products qualities.

PLAL for the production of VO_2 have not been reported despite some attempt to produce vanadate nanoparitlces by Bezerra et al. [12]. Pulsed laser ablation in liquid (PLAL) is a technique which uses a high intensity laser pulse to irradiate solid material target submerged in a liquid medium. After irradiation, plasma with high temperature and pressure is released. The plasma then interacts with the liquid. The interaction of plasma with liquid interface causes oxidation.

PLAL method offers certain benefits to control the size of the nanoparticles by varying wavelength, laser pulse duration, irradiation of nanoparticle colloid and changing solvent type [13]. PLAL method is an environmentally friendly process, offering a wide range of benefits over conventional synthesis. PLAL generates nanoparticles at room temperature, it is considered a one-step synthesis method, nanoparticles synthesized by this technique have extensive morphologies, dimension and phases, it produce chemically clean products, it offers a low cost experimental technique and provides a high pressure and high temperature confinement which allows formation of unique products. Furthermore, PLAL enables fabrication of particles from various solid state precursors such as metals, alloys, oxides, carbides and hydroxides [14], [15].

The main aim of this thesis is to investigate synthesis methods for VO_2 nanoparticles by PLAL. For this purpose, 99.8 % pure vanadium (V) metal-target submerged in liquid is ablated by a high frequency fiber laser ($\lambda \approx 1060$ nm, pulse width 20 ps, repetition rate one MHz). To achieve the synthesis of vanadium oxide different liquids have been used. The selection of liquids was performed cautiously to avoid unwanted reactions due to high reactivity of vanadium. The liquids used in the experiment are acetone, alcohol, acetonenitrile, pyridine, 2-propanol, methanol, hydrogen peroxide and water. SDS (Sodium dodecyl sulphate) was used as a surfactant.

This thesis is divided into two main parts. The theoretical part deals with the background information which is relevant to the experimental work, topics include vanadium's physical and chemical properties, pulsed laser ablation, characterization techniques. Under the properties of vanadium oxides, different oxide structures are briefly presented. Understanding the different oxide structures is vital since most of the properties, characterization and applications depend on the structure. The second part deals with experimental findings.

1. THEORETICAL PART

1.1 Laser Ablation in Liquid

Laser is light amplification by stimulated emission of radiation. An ideal laser produces coherent, monochromatic electromagnetic radiation with a wavelength from ultraviolet to infrared. Laser ablation is defined as the process of removing materials from a solid surface by laser irradiation. “Ablation” is derived from a Latin word “ablatio” which means removal [16].For the first time in 1987, Patil and his associates used pulsed laser ablation in liquid (PLAL) to produce metastable iron oxide [16]. During PLAL a high power laser beam is focused on to the surface of a solid target which is submerged in a liquid medium. The interaction of the laser with the target causes vaporization of materials in the form of plasma plume; which constitutes of atoms, ions and clusters. The high temperature plasma plume expands by exerting pressure on the liquid interface. The expansion is confined by the surrounding liquid leading to the formation of cavitation bubble. As a consequence, a state of higher pressure, higher temperature, and higher density confinement will be created. The temperature of the plasma plume formed during PLAL is estimated between 4,000-6,000 K and pressure can be around 10 GPa [17-19].

During PLAL, the main reaction initiated can be classified in two phases: laser induced ablation plasma plume and plasma induced plasma plume. Plasma induced plasma plume is created by further laser induced plasma plume (i.e liquid turned into plasma plume by plasma). During laser induced plasma plume and plasma induced plasma plume, there will be a reaction of the ablated particles at high temperature and pressure. The reaction occurs between the particles of the ablated target and the liquid interface. This distinctive reaction environment is expected as an ultimate condition for discovering unique materials [18], [19]. In this stage, meta-stable compounds could be formed [18] , [20].

As shown in Figure 1.1, after the cavitation bubble reached the threshold it will collapse. Consequently, a shockwave will be released to the ambient liquid which can create secondary cavitation bubbles. Based on the explanation by Sasaki et al. the secondary cavitation bubbles sometimes might not disappear depending on the laser parameter used [21]. Thus, the formation of bubbles and shockwaves cause a change in the refractive index, leading to refraction of the laser beam which decreases the efficiency of the ablation process [22].

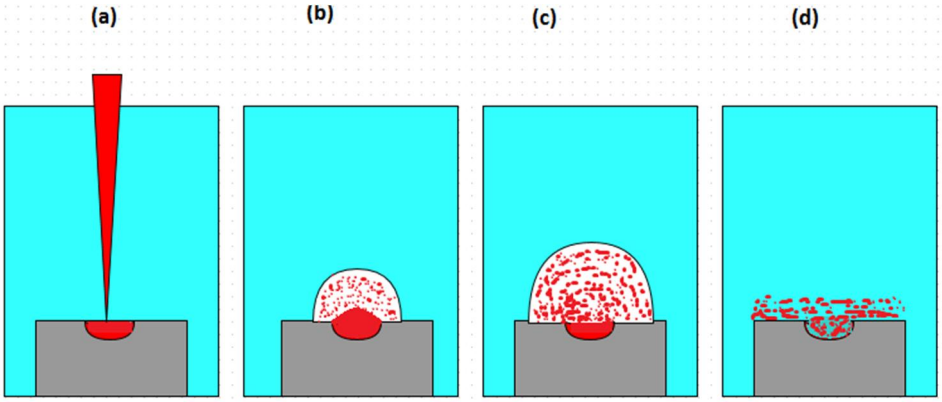

Figure 1.1 Schematic diagram showing progress of irradiation by PLAL (a) laser interaction with the target (b) development of plasma (c) cavitation bubble comprising condensation of vapours (d) cavitation bubble quenching (figure modified from [23])

Sasaki et al. [21] have studied the growth dynamics of nanoparticles during PLAL. In the experiment, images of PLAL have been taken by measuring the amount of scattered laser light as shown in Figure 1.2. Based on the image, after 7 μs of the ablating laser pulse, scattered light is observed indicating nanoparticles in the cavitation bubble. The strongest scattering from the nanoparticles is observed at the interface of the cavitation bubble and the liquid which suggest the particles grow at the interface [21]. After the cavitation bubble collapses, the particles disperse as colloids.

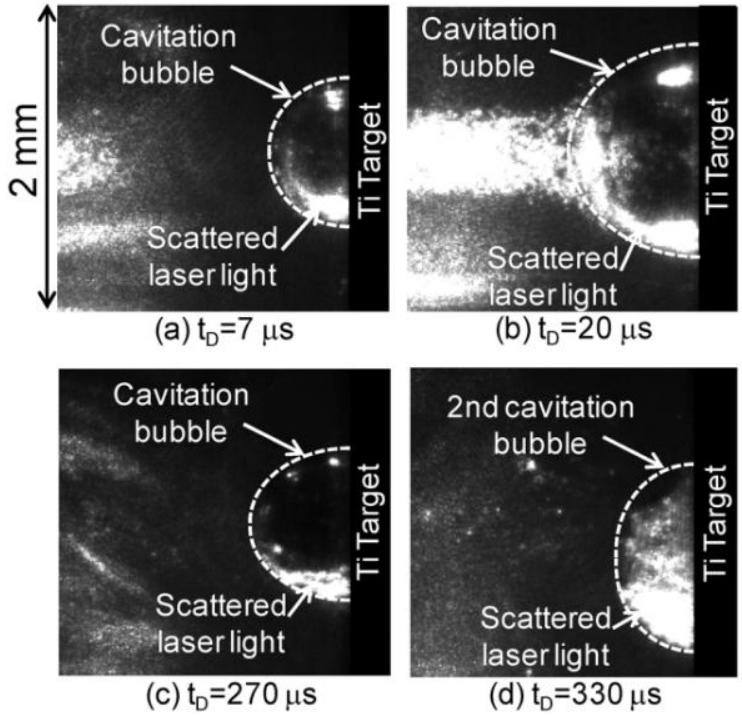

Figure 1.2 In situ detection of scattering laser light by nanoparticles (a) expansion of the cavitiation bubble (b) nanoparticles escaping the cavitation bubble. (c) high density nanoparticles before the collapse of the cavitation bubble. (d) Secondary cavitation bubble created by the collapse of the principal cavitation bubble with higher concentration of nanoparticles [21].

1.1.1 Colloids Stability

Colloids are solutions of particles with size range from 2 nm to1000 nm. The particles in the colloid may collide to form an aggregate. Aggregation and precipitation effect depends on the zeta (ζ) potential. Zeta potential is a potential difference created when a nanoparticle attracts particles with an opposite charge, forming a thin layer of ions as shown in Figure 1.3. The ions closer to the charged particle form strong attraction Stren layer which move with the particle. The second layer, slipping plane, formed by ions attracted by the coulomb force does not move with the particle. The potential difference at the interface between the bulk liquid and the slipping plane is called ζ-potential [24].

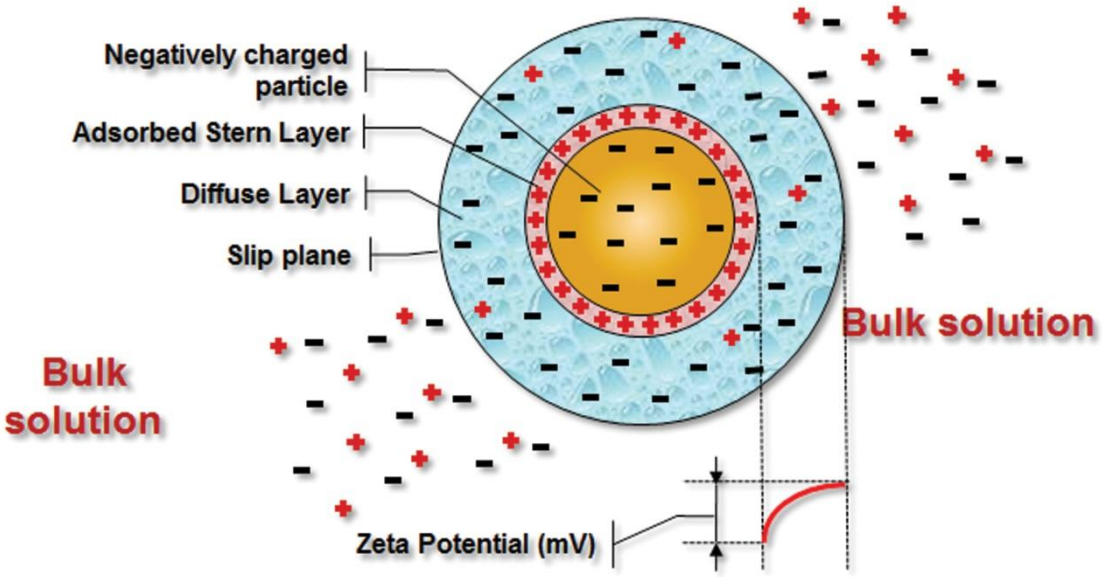

Figure 1.3 Schematic diagram showing charge distribution around a particle with surface charge [25]

Stability of colloids can be predicted by analysing the ζ- potential. For ζ- potential ∓(0-5) mV particles tend to agglomerate, ∓ (5-20) mV particles are minimally stable, ∓(20-40) mV particles are moderately stable. Higher stability colloids found within ζ potential greater than +40 mV or less than -40 mV [26], [24].

ζ - potential can be manipulated by adjusting the pH of the solution or adding ionic particles such as salts. Furthermore, addition of surfactants (surface active agents) which adsorb to the surface of the particles will modify the charging phenomena [27].

The pH value at which the net charge of the particles is neutralized is called isoelectric point. At this point, the colloid suspension will precipitate. To measure the zeta potential, the most commonly used method is electrophoresis. Electrophoresis is based on electrophoretic mobility and it also used as a coating technique. More detailed explanation of the use of electrophoresis for deposition is discussed under the chapter 1.3 (Electrophoretic Deposition).

1.1.2 PLAL Experimental Setup

Instrumental arrangements for PLAL differ based on the experiment. Calvo [28] has classified the fundamental arrangements into three categories as shown in Figure 1.4. In these arrangements a laser is focused onto a solid material, which is submerged in a liquid. As Calvo has suggested, focusing laser at the free surface of the liquid is advantageous to reduce reflection [28].

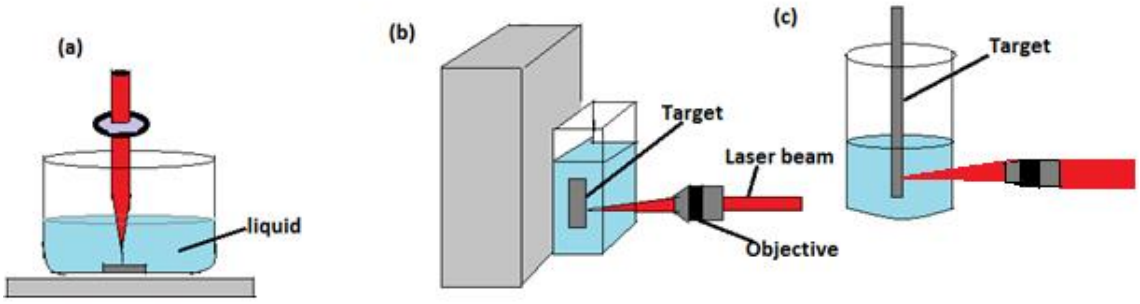

Figure 1.4 (a) The solid target placed at the bottom of a beaker or cuvette. (b) The solid target suspended in vertical direction (c) Arrangement for ablating rod or wire target,(The figure is slightly modified from [28]).

The schematic diagram in Figure 1.4 (a) shows the simplest setup with the target placed at the bottom of a container. To prevent crater formation, either the sample or the laser should move (for instance, in horizontal direction or circular direction). The arrangement shown in Figure 1.4 (a) is the least applicable method due to its lowest yield. This is due to the highest effect of bubbles diffracting laser beam, and laser focusing is affected by the ablated particles. To reduce laser beam scattering by the bubbles and increase production rate a constant liquid motion is advisable. Much higher performance is achieved by creating an arrangement of flowing liquid, for instance using magnetic stirring as shown in Figure 1.5. Barcikowski et al. [29] have reported femtosecond laser ablation of silver with the same laser parameters in stationary and flowing liquids. The results showed production rate increase for the flowing liquid by four times compared to the stationary liquid. In addition, reproducibility of the experiment was improved [29].

The schematic diagram in Figure 1.4 (b) shows arrangement used for this thesis. In this arrangement the target is suspended vertically while the laser beam is rastered horizontally.

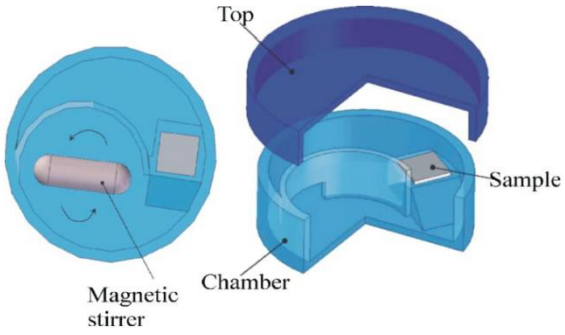

Figure 1.5 Specially constructed stirred chamber. Figure copy righted and reprinted from [29], with kind permission from AIP publishing LLC

1.1.3 Influence of the Laser Parameters

Lasers used in PLAL have wavelength in the visible or the near infrared region of the spectrum. The main criterion for the selection of the laser wavelength is based on the transparency of the solvent. According to Yang and Guowel [30], various laser sources can be used, such as Nd:YAG laser, Cu vapor laser, and Ti: sapphire laser. To ensure peak laser power the laser is focused on the target.

During laser irradiation of a solid metal target, energy is absorbed by free electrons. The energy is transferred by relaxation to the lattice, this thermal relaxation occurs predominantly at the laser spot. Transfer of energy from electrons to the lattice occurs rapidly in the order of few picoseconds. When the energy absorbed from the laser pulse is above the ablation threshold it will cause plasma [22], [32-34]. Based on calculation made by Shafeev [31], the temperature inside the spot can be estimated as shown in eq. 1.

$$T \approx \frac{AF}{c\rho h} \tag{1}$$

Where A is absorption (A= 1-R), R is the reflectivity coefficient, c is the heat capacity, ρ is the density, h is the heat diffusion length and F is the fluence (energy per area). As can be seen from the eq. 1, the temperature is directly proportional to the fluence. Further quantitative analysis made by Shafeev suggests increasing the duration of the pulse leads to increased laser heating depth [31].

The ablation mechanism in PLAL differs based on fluence, solid material properties, pulse repetition rate and pulse duration. The laser pulse duration ranges typically from hundreds of femtosecond to nanoseconds. Ablation of material by nanosecond pulses is mainly a thermal process. This is because of the longer pulse duration; the transfer of energy from the electrons to the lattice occurs during the laser pulse duration. The electrons and the lattice are in thermal equilibrium. Thus, the lattice has time to react to the pulse by heat conduction, melting, evaporation and plasma formation. However, in case of ultra-short laser pulses (picosecond and femtosecond) the laser pulse duration (T_L) is shorter than the lattice heating time (T_i) ($T_i > T_L$); the electrons and the lattice are not in thermal equilibrium. In ultra-short laser pulse, plasma plume occurs after the laser pulse as shown in Figure 1.6 [22], [33-34].

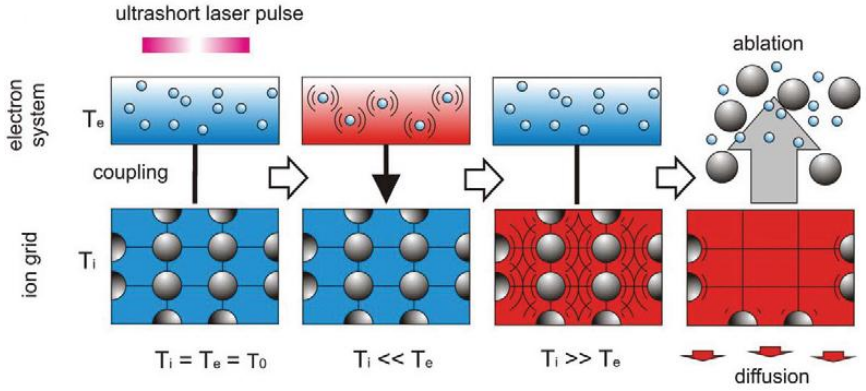

Figure 1.6 Schematic diagram of ultrashort laser pulses. Figure slightly modified, copy righted and reprinted from [35], with kind permission from physics procedia.

By keeping the same fluence and changing laser pulse duration, it is possible to influence the size distribution of nanoparticles. To improve uniformity of the size distribution, preferred laser pulses are within the range of nanoseconds. Nanosecond laser pulse has the tendency to coexist with the ablated materials for relatively long time. The extended time helps part of laser energy to further evaporate melted particles to plasma plume [36].

For producing more nanoparticles irrespective of the size distribution, a higher picosecond laser power produces more particles than femtosecond laser power. Although, in terms of efficiency the femtosecond laser ablation is 20 % more efficient than picosecond laser ablation. Barcikowski et al. [31] have observed the productivity of Ag nanoparticles with picosecond pulse laser is higher than femtosecond laser. Production rate for the picosecond laser was 3.4 times higher than for the femtosecond laser; for the same pulse fluence. For commercial production of Ag nanoparticles a 6 Watt picosecond laser can generate 34 mg/h while a femtosecond laser with 3 Watt average power can produce 6 mg/h.[1] [31].

Increasing the pulse repetition rate increases the rate of nanoparticle generation considering each pulse generates nanoparticles with the help of a fast scanning of the laser beam. Pulse repetition rate (pulse repetition frequency) is the number of emitted pulses per second. A linear correlation between ablation rate and production occur within the pulse repetition rate lower than 10^3-10^4 Hz [36]. However, at higher pulse repetitions rate cavitation bubbles reduce laser efficiency due to scattering, since previously created cavitation bubbles from earlier pulse remain covering the target [31], [36].

In PLAL higher pulse energy increase the rate of ablation; considering the ablation mechanism remains the same. Increase in pulse energy result different process to take place at the same time; for instance, melting, boiling or photoionization. Increasing ablated materials concentration at higher pulse energy lead to formation of large nanoparticles. The higher the pulse energy, the more non-uniform size distribution will be formed as a result of multiple processes taking place at the same time [36].

1.1.4 Oxide Nanoparticles Synthesized by PLAL

This topic deals with a brief review of metallic oxides synthesised by PLAL. Most studies of PLAL deals with noble metal nanoparticles. Some studies have also been done on metal oxides. Metallic oxide of hollow nanoparticles, nanocubes, nanospheres have been synthesised for metals such as Cu, Co, Zn, Ti, Ce, W, In and Al as summarized in Table 1.1.

During metallic oxides synthesis various methods can be used to control size, morphology and reactivity. For instance, as T. Sasaki et al. [37] have demonstrated size of metallic oxide nanoparticles can be decreased by using sodium dodecyl sulfate (SDS: $C_{12}H_{25}SO_4Na$). Addition of SDS aids to synthesis TiO_2 and SnO_2 nanoparticles within

[1] these results suggest the extrapolation estimation is nonlinear

size range of 2 to 6 nm [37]. Surfactants which attach to the metallic oxide surface prevent particles growth. Furthermore, surfactant such as lauryldimethylaminoacetic acid betaine has also shown to affect photoluminescence of ZnO (no luminescence in the presence of the surfactant) [42].

Morphology of metallic oxide nanoparticle is also affected by the laser energy. According to Kebede et al. [38], increasing the ablation energy in preparation of iron oxide leads to production of triangular nanoparticles instead of the spherical nanoparticles [38].

Table 1.1. Metallic oxides synthesized by laser ablation in liquid [39-44]

Target	**Liquid**	**Volume ratio**	**Product**
Mg	n-hexane:ethanol	1:0, 5:1,0:1	Mg/O [2]MNPs/[3]HNPs/[4]NCs
Cu	Water:ethanol	5:1	Cu/O HNPs
Co	Water:ethanol	10:1	Co/O HNPs
Co	Water		Co_3O_4/ nanoparticles
Fe	Water:ethanol	5:2	Core/hollow shell [5]NSs
Zn	Water:ethanol	1:10, 1:8, 1:6	Core/shell NSs
Zn	H_2O+ 3%H_2O_2		ZnO_2/nanoparticles
Zn	water +[6]LDA, Water +		ZnO/nanoparticles
Zn	[7]OCM		Zn+ ZnO/ nanoparticles
Zn	Water, Water +SDS		β-$Zn(OH)_2$/layered nanocomposite
	Water + [8]SAS		
Ti	Water:ethanol	1:3, 1:5	Core/shell NSs
Ti	Water, water +SDS		TiO_2/amorphous, anatase
Sn	Water		Sn+ SnO_2/ nanoparticles
	Water+SDS	1 x 10^{-2}M SDS	SnO_2 /nanoparticles
W	Water		WO_3
In	Water		In_2O_3
Al	Water		$Al(OH)_2$, AlOOH/ amorphour
Al	Water + NaOH	0.05M-1M NaOH	Mixture of β-$NaAlO_2$ and γ-Al_2O_3
Mg	Water, water+SDS		$Mg(OH)_{2/}$ Tubular and spindle
Ga	Water+ [9]CTAB		GaOOH
Mn	Water		Mn_3O_4
Sb	Water		Sb_2O_3 nanoparticles
Ni	Water+SDS	0.5M SDS	NiO nanoparticles

[2] MNPs - Mg nanoparticles,
[3] HNPs - Hollow nanoparticles
[4] NCs - nanocubes
[5] NSS - nanospheres
[6] LDA - Lauryl dimethylaminoacetic acid betaine
[7] OCM - Octaethylene glycol monododecyl ether
[8] SAS - Sodium alkyl sulfates
[9] CTAB - Cetyltrimethylammonium bromide

1.1.5 Advantages and Disadvantages of PLAL

PLAL offers various advantages; first it is an environmentally friendly method. Since nanoparticles generated by PLAL are kept in the solvent. Thus, airborne particles from PLAL are not an issue for work safety. Second, nanoparticles are generated in the solvent which simplifies further processing. Moreover, presence of properly selected solvent inhibits agglomeration of the particles. Agglomeration is challenging for methods that lead to production of dry nanopowders. Third, the process generates pure nanoparticles, which are free from impurities or toxic elements. Pure nanoparticles are generated when the solvent is free from any additives (such as stabilizers, acids, bases, oxidizing agents). Thus, the pure products might be used for instance, for demanding medical applications [45]. Fourth, the size of the particles could be adjusted by varying the laser parameter and liquid type. For instance, by reducing laser wavelength it is possible to decrease particles size. That is femtosecond laser pulses generate smaller particles than nanosecond laser [46]. In addition, size of particles could also be controlled by applying an external pressure as Soliman et al. [47] have demonstrated for size control during the synthesis of ZnO. However, size control is more practical and precise in chemical methods than in PLAL. Fifth, PLAL offers technical simplicity with low running costs. Sixth, the particles generated by PLAL usually have a positively charged surface. This charged surface could be used for functionalization of particles. For instance, the positive charge could be conjugated with electron donating compounds. This conjugation could be efficiently performed between nanoparticles and biomolecules. The nanoparticle-biomolecule conjugate could be used for biomedical application such as bioimaging, drug targeting, and for quantitative intracellular detection [23], [45].

While considering shortcoming of PLAL, initial laser equipment might be expensive and production rate is relatively low, in the order of mg/h. In order to increase the scale of production some working parameters might be adjusted such as ablation time, laser irradiance, repetition rate and liquid parameters (surface tension, viscosity) [36].

1.2 Vanadium

Vanadium was discovered for the first time in Mexico in 1801 by Andres Manuel del Rio. However, it was considered contaminated chromium; thus the discovery was ignored. Afterward, it was then rediscovered by a Swedish Chemist Nils Gabriel Seftström in 1830. He named the element after the Norse goddess Vanadis, which represents beauty and fertility due to vanadium's colourful compounds. In 1867, the first pure vanadium metal was produced by reducing vanadium chloride with hydrogen [48]. Vanadium is a transition metal of group V of the periodic table, which consists of Niobium (Nb) and Tantalum (Ta). It is silver-grey metal found in various minerals such as carnotite and vanadinite. It has atomic number of 23 with electron configuration of [Ar] $3d^3 4s^2$, atomic weight 50.9415, it has two isotopes ^{50} V and ^{51}V. In nature, the most

abundant isotope is ^{51}V (at around 99.8%). ^{50}V is slightly radioactive with a half-life of $6x10^{15}$ years. Within the group, vanadium is the least electropositive element with stronger metal-metal bonding, resulting in high melting point (1915 ℃) and boiling point (3350 ℃). Compared to other transition metals such as iron (or steel), it is considered as a harder metal (but not brittle), ductile and malleable [49], [50].

Vanadium exists in nature along with other elements (K, Ca, Mg, Pb, Al, P, Cl, Fe, Si and Mn) in 54 different ores, for example Vanadinit $Pb_5[VO_4]_3Cl$, Roscoelite ($KV_2(OH)_2/AlSi_3O_{16}$), Descloizite (Pb(Zn,CU)[OH/VO_4], Montroseite ([V,Fe]OOH) [51], [52].

Purification of vanadium is challenging because of the diverse impurities. Some of the methods used are calcium reduction, thermal decomposition, solvent extraction and electrolytic refining. For instance since 1900s, a purification method by reduction reaction between vanadium pentoxide and calcium metal is used [51], [52].

Figure 1.7 $Pb_5[VO_4]_3Cl$ (Vanadinit) ore of vanadium consisting of Pb and Cl as impurities [53]

Vanadium resists reaction with alkalis, sulfuric acids and hydrochloric acids. Complete oxidation of vanadium by air is only achieved at elevated temperature; around 933 K (660 ℃). At temperature below 250 ℃ vanadium is unreactive. Though, the surface might oxidize showing visible colour change from bluish grey to brownish black. Vanadium initiates oxidation in air above 300 ℃ and absorbs hydrogen into the lattice sites until 500 ℃ . At higher temperature, it will react with other elements. For instance, above 800 ℃ it reacts with nitrogen and carbon to form vanadium nitrides, and carbides (800-1000 ℃) [51-54].

As shown in Figure 1.8, vanadium is used in various forms, for instance it is added in steel as an alloy to increase strength, resistance to corrosion and as sample holder for neutron diffraction. The first vanadium steel alloy was manufactured in 1903 in England. In 1905 Henry Ford used vanadium steel alloy for car manufacturing. Thus, he could reduce the car's weight by 50 % [51-54] In the future, vanadium can be used for green technologies such as in batteries for electric cars.

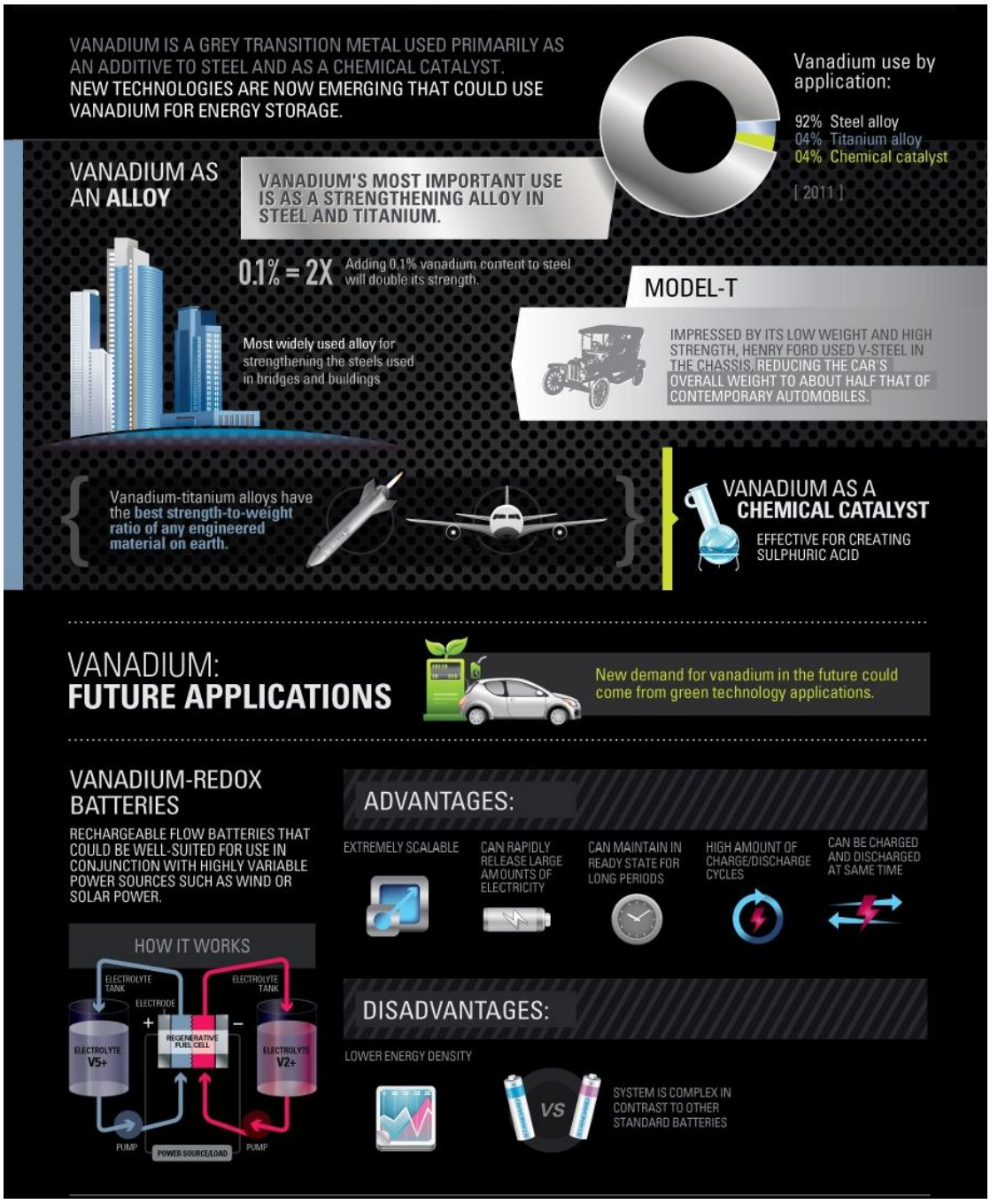

Figure 1.8 The primary application of vanadium is for strengthening steel and titanium alloys. In the future it can be used for rechargeable batteries. Figure is slightly adapted from [55]

1.2.1 Vanadium Oxide Properties

Oxidized vanadium has resistance to dilute sulfuric acid, hydrochloric acid and phosphoric acid. Though, lower resistance/dissolves in nitric acid and hydrofluoric acids. Vanadium oxides resist sodium hydroxide to a certain extent (about 10 %). Whereas, it will react with hot potassium hydroxide [52], [54]. The wide variety oxidation states of vanadium leads to a wide range of oxides. Oxides of vanadium exhibit a complex stoichiometric composition. For instance, vanadium can exist as a mixed oxidation state such as +5 and +4 coexist in V_6O_{13}; mixed oxidation of +4 and +3 are observed in V_8O_{15},V_7O_{13},V_6O_{11}. Stable vanadium oxides are in the range of 15-20. About 8 of vanadium oxides show a reversible phase transition; these oxides are V_2O_3, VO_2, V_3O_5, V_4O_7, V_5O_9, V_6O_{11}, V_2O_5 and V_6O_{13} [56]. Concerning this thesis the most interesting oxides are VO_2 and V_2O_5.

Oxides of vanadium are used as catalysts. V_2O_5 for instance, is used as an industrial catalyst for the production of sulfuric acid during conversion of SO_2 to SO_3 by contact process. V_2O_5 has replaced expensive platinum catalyst which was previously used for oxidation. Consequently, it has reduced the cost of sulfuric acid production. Furthermore, V_2O_5 is known for its catalytic oxidation of organic compounds in the presence of air or hydrogen peroxide, it acts as a catalyst for reduction of alkenes (olefins) by hydrogen [52], [54].

V_2O_5 exhibits amphoteric property which is slightly soluble in water (0.1-0.8g/100 cm^3) [57]. In acidic solutions, it will dissolve to form yellow $[VO_2]^+$ ions while in basic solution, it will form colourless VO_4^{3-} ions. Similarly, VO_2 is amphoteric oxide, which dissolves in reducing acids forming blue $[VO]^{2+}$, whereas in basic solution, it develops $[V_4O_9]^{2-}$ ion with characteristic colour of yellow to brown. If the solution basicity (pH) increased further, then $[V_4O_9]^{2-}$ is converted into $[VO_4]^{4-}$. Whereas, V_2O_3 is basic oxide, it is soluble in acidic aqueous solutions [52].

V_2O_5 displays electrochromic properties with varying colour from blue to green and yellow within two seconds upon charging/discharging. Electrochromic materials change their optical properties reversibly during electrochemical reactions. These materials are used for smart windows, display devices and controlled reflectance mirrors [58]. The working mechanism of electrochromic materials consists of electrolyte, intercalated mobile ions which performs intercalation/deintercalation while a potential difference is applied. For this purpose, layered structure of V_2O_5 is a promising material [59].

All oxidation states of vanadium (+2 to +5) can exist in aqueous solution. Oxidation state of +4 and +5 create VO_2^+ ions by interacting with water and liberating H^+ ions; turning the solution acidic. In aqueous solution, different oxidation states can be recognized from the colour of the solution as shown in Table 1.2. The most familiar oxidation states of vanadium are +2 (violet), +3 (green), +4 (blue) and +5 (yellow). As the oxidation state increases, the compound becomes an oxidizing agent. Lower oxida-

tion states are reducing agents. For instance, +5 is an oxidizing agent and +2 is a reducing agent [52], [60].

Table 1.2. The most common oxides of vanadium colour and critical transition temperature [61-64]

Compound	Colour of the compound	Transition temperature	Ion	Colour of the Ion	Oxidation state
V_2O_5	Orange Yellow	+375℃	VO_3^-/ VO_2^+	Yellow	+5
VO_2	Dark blue	+67℃	VO^{2+}	Blue	+4
V_2O_3	Black	-105℃	V^{3+}	Green	+3
VO	Grey	-147℃	V^{2+}	Violet	+2

Colour of the aqueous solutions of vanadium oxide is pH dependent. If V_2O_5 is dissolved in an aqueous solution containing base, like NaOH, then the colour of the solution change to colourless. However, colour might be visible after the solution pH gradually decreases to acidic solution. The colourless solution gradually become slightly light yellow then it will change to orange colour. During these transformations, orange colour gradually turn to red indicate charge neutrality point. The colour further darkens and at pH two precipitate of V_2O_5 formed. If the pH is decreased further, then the particles dissolve again producing a pale yellow solution. Thus, transformations of V_2O_5 to colourless implies formation of VO_4^{3-} and the final pale yellow colour is due to the formation of VO_2^+ ions [52].

1.2.2 Structures of Vanadium Oxides

Vanadium forms various morphologies with different coordination arrangements. The most common coordination arrangements are: tetrahedral (VO_4), trigonal bipyramids or square bipyramids (VO_5), distorted and regular octahedrons (VO_6) [65].

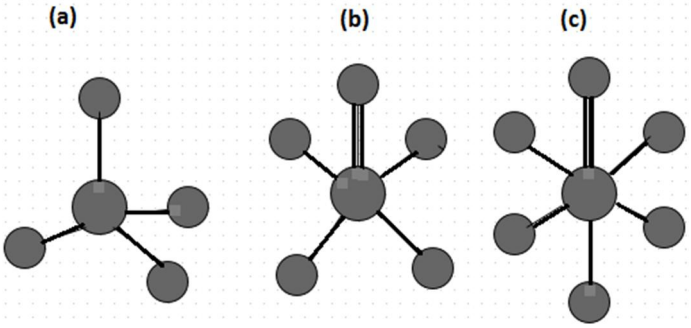

Figure 1.9. Common vanadium oxide coordination structures (the centre atom represent vanadium) (a) Tetrahedron, (b) Square pyramid, (c) Octahedron

Frequent oxides coordination of 4, 5 and 6 are displayed in Figure 1.9. Tetrahedral coordination is a preferred arrangement for +5 oxidation state [65].

According to Elisa et al. [66], there are two bulk structures α-V_2O_5 and γ-V_2O_5. The structure of α-V_2O_5 has an orthorhombic layered structure. Pyramid structural arrangement builds with five oxygen atoms surrounding one V atom. The edge corners of the pyramids are shared along the chain as shown in Figure 1.10. The oxygen atoms have different coordination depending on the position. There are three possible oxygen positions: the first position is the oxygen acting as a link between two vanadium atoms; the second is between the layers as a bridge and the third oxygen position is situated in three coordination sites. The oxygen between the layers exerts a weak Van der Waals force to bind layers, which is easily detachable [66].

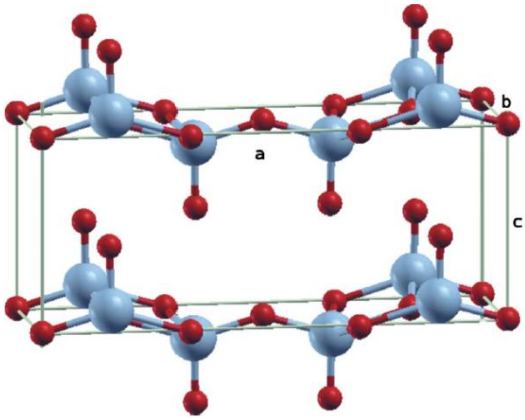

Figure 1.10 α-V_2O_5 structure where V atoms are represented by larger ball and O atoms by the red small balls. The letters a, b, c represents the orthorhombic unit cell. The oxygen in between the layers is responsible for the weak Van der Waals force which binds the layers together. Figure copyrighted and reprinted from [66], with kind permission from Prof. Elsebeth Schröder and the American physical society.

The structure of vanadium pentoxide (V_2O_5) exhibits intercalation layered structure. As a result, it offers a possibility of reversible intercalations of different atoms, molecules or ions. The interlayer separation of V_2O_5 changes depending the size and shape of the intercalated particles [67].

One of the applications of V_2O_5 is as an electrode for lithium batteries cathode materials. For this application, Li - ion intercalated as shown in eq. 2 [67].

$$V_2O_5 + xLi^+ + xe^- \leftrightarrow LixV_2O_5 \qquad (2)$$

The state of V_2O_5 for Li battery can be crystalline, xerogel or aerogel ($V_2O_5.nH_2O$). Li ion intercalated V_2O_5 is used to reduce the cost, simplifies the synthesis method, and to improve the energy density [68]. More information regarding the use and properties of V_2O_5 for lithium ion batteries are explained by Staley [68].

The structure of VO_2 is discussed in section 1.2.6 (Semiconductor to metal phase transition of VO_2).

1.2.3 Xerogels

Xerogels ($V_2O_5.nH_2O$) are usually observed in an aqueous solution as a red gel during the synthesis of V_2O_5 with oxide coordination as shown in the molecular structure of Figure 1.11. The ribbon like xerogels usually have 1 μm length and 10 nm diameter. According to atomic pair distribution functional study by Valeri et al. [69], xerogel structures show different structure than V_2O_5. Xerogel is constructed through layer piling up of V_2O_5 in the c-axis of monoclinic unit cell as shown in Figure 1.12. Though, no regular order on the stacking arrangement [69]. Different researchers have proposed various possible structures. Because of the lack of crystal properties, the atomic structure is challenging to predict [70].

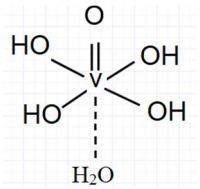

Figure 1.11 $V_2O_5.nH_2O$ gels

$V_2O_5.nH_2O$ shows various properties such as magnetic field alignment, gel elasticity, redox and intercalation properties. These properties can be used in various applications, for instance in a photographic industry, in batteries and in electrochromic displays. Xerogels are stable forms of amorphous and crystalline V_2O_5 in an aqueous solution [71].

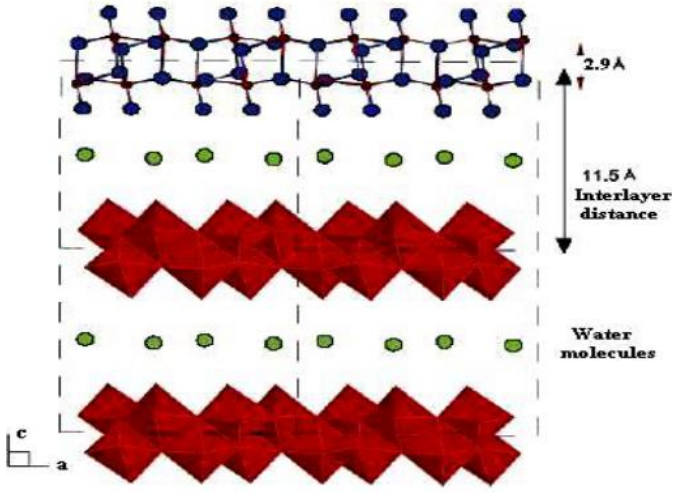

Figure 1.12 Ribbon like xerogel structures from pair distribution function technique study, green indicate the water molecule. Figure copyrighted and reprinted from [69], with kind permission from American Chemical Society.

Water content in $V_2O_5.nH_2O$ affects the conductivity and electrochemical phenomena. It is easy to remove water molecules by thermal annealing, thus conductivity increase with few significant alternation on morphology. As Barbosa et al [72] reported the complete removal of water occurs at a temperature of 600 ℃. Based on the report,

progressive annealing of xerogel V_2O_5. 2.1 H_2O in air at temperature of 150 ℃, 270 ℃, 600 ℃ for 15 min result V_2O_5. 1.1 H_2O, V_2O_5.0.32 H_2O and V_2O_5 respectively [72].

1.2.4 Vanadium in Aqueous Solution

In aqueous solutions, the composition of vanadium solute and ions can be altered either by adjusting the concentration or Ph as shown in Figure 1.13. Aqueous chemistry of vanadium has been studied by different scholars from the perspective of biological molecule [73], [74]. This topic briefly discusses the interaction of vanadium in an aqueous solution excluding the biological aspect. The discussion will focus on the oxidation states of +3, +4 and +5.

Oxidation state of +5 is called vanadate. Vanadate at around neutral pH will exist mostly as a mono anion ($H_2VO_4^{1-}$). The lower oxidation states +2 and +3 are found as conjugate of water molecules $[V(H_2O)_6]^{2+}$ and $[V(H_2O)_6]^{3+}$ respectively. As the oxidation number increased, the water ligands around V metal gradual release hydrogen ions [74].

$$[V(H_2O)_6]^{3+} \rightleftharpoons [V(H_2O)_5(OH)]^{2+} + H^+(aq) \quad pKa = 3.5$$

Depending on the oxidation state and pH; proton donation of water-vanadium complex might be in equilibrium or irreversible reaction. In case of acidic solution, for instance the +4 and +5 oxidation state will be irreversible (stable). This high stability of oxycations in concentrated acidic solution is achieved by liberation of protons from aqua complexions [74].

Irreversible » $[V(H_2O)_6]^{4+} \rightarrow [VO(H_2O)_5]^{2+} + 2H^+_{(aq)}$

Irreversible » $[V(H_2O)_6]^{5+} \rightarrow [VO_2(H_2O)_4]^{1+} + 4H^+_{(aq)}$

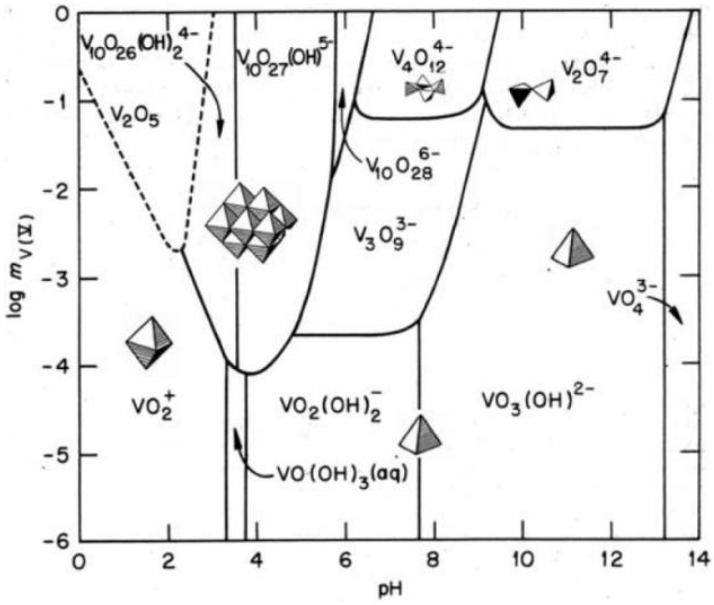

Figure 1.13 The various stages of vanadium solute and ions in aqueous solutions depending on the concentration and pH. Figure copyrighted and reprinted from [75], with kind permission from Materials an open access journal.

The aqueous interaction further complicated by instability of the oxidation state. For example, in neutral and basic pH, vanadate acts as an oxidizing agent reducing to +4 or +3 state. However, air oxidation restores vanadate, unless it is stabilized by ligand. [74].

In aqueous solution, the increment in acidity from de-protonation of water molecules from $[V(OH_2)n]^{5+}$ is summarized as follows [75]:

$$[V(OH_2)_6]^{5+} + hH_2O \rightarrow [V(OH)_h(OH_2)_{6-h}]^{(5-h)+} + hH_3O^+$$

As the value of h increases vanadium ligands with aqua change to hydroxo and then oxo-species. The state of equilibrium is achieved when the average electronegativity of the hydrolyzed vanadium precursors ($\chi_p = [V(OH)_h(OH_2)_{6-h}]^{(5-h)+}$) equals to the electronegativity of the aqueous solution. In the equilibrium region protons are delocalized uniformly over the hydrogen bonds. Thus, the electronegativity of pure water and hydronium ion is neutralized [75].

If the concentration of vanadium is high enough, two possible condensations paths arise (olation and oxolation). These condensations, olation and oxolation, occur by merging vanadium cations (V^+) with the hydroxide groups (OH^-). In terms of kinetics, olation is faster than oxolation because there are more water ligands than hydroxide. Thus, precipitation of vanadium pentoxide (V_2O_5) can be achieved at a point of zero charge. Approximately, around Ph ≈ 2 from the condensation of $[VO(OH)_3(OH_2)_2]$ [75].

$$\text{-V-OH + -V-OH}_2 \rightarrow \text{-V-OH-V- + H}_2\text{O} \qquad \text{(Olation)}$$
$$\text{-V-OH + HO-V-} \rightarrow \text{-V-O-V- + H}_2\text{O} \qquad \text{(Oxolation)}$$

V_2O_5 precipitates as red brown gelatinous hydrated vanadium pentoxide $V_2O_5.250H_2O$ around pH 2. Above pH 2, it will form a complex of polyvanadate with yellow color. In basic solution at around pH 10, a colorless metavanadate (VO^{3-}) anion formed. If V_2O_5 is dissolved in basic solution it will create VO^{2+} complex again [76].

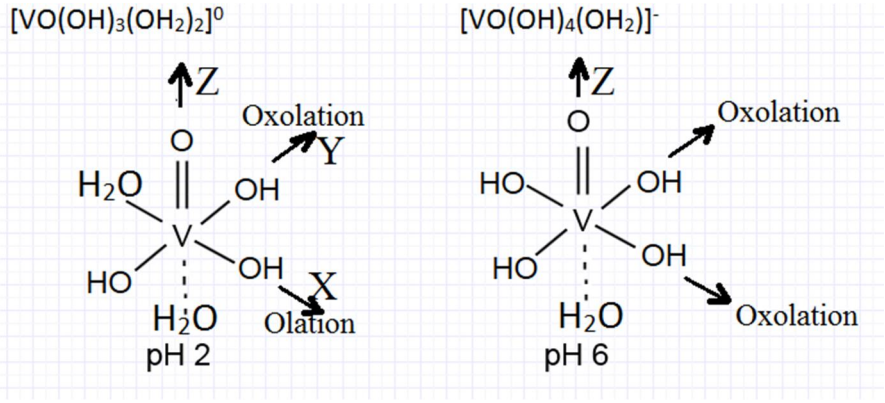

Figure 1.14 Vanadium aqueous molecular structures

A computer simulation made by Chernenko et al. [77] suggest some procedures for synthesis VO_2 in a supersaturated solution. To produce vanadium products as less soluble particles, it is advisable to use additional highly soluble components such as a base or an acid. The chemical composition selected for the analysis was aqueous solution of V_2O_5 in the presence of sulphuric acid (H_2SO_4) and sodium hydroxide (NaOH). These chemicals were selected based on the fact that V_2O_5 is slightly soluble in water (0.07 g/100 g of H_2O at 25 ℃), whereas VO_2 is insoluble [77].

Thus, the analysis aims at understanding the Gibbs isobaric-isothermic potential of minimum value. The temperature and pressure are kept at normal atmospheric condition. The prepared aqueous solutions for both V-O-H-S and V-O-H-Na consist of tetravalent ions (VO^{2+}) and pentavalent ions (VO_4^{3-}, $H_2VO_4^-$,VO_2^+ and others). The significant differences between the two solutions are the vanadium components. Pentavalent vanadium is abundant in the V-O-H-S solution, for instance V_2O_5, H_3VO_4,VO_2^+, VO_4^{3-}, HVO_4^{2-} as shown in Figure 1.15 [77].

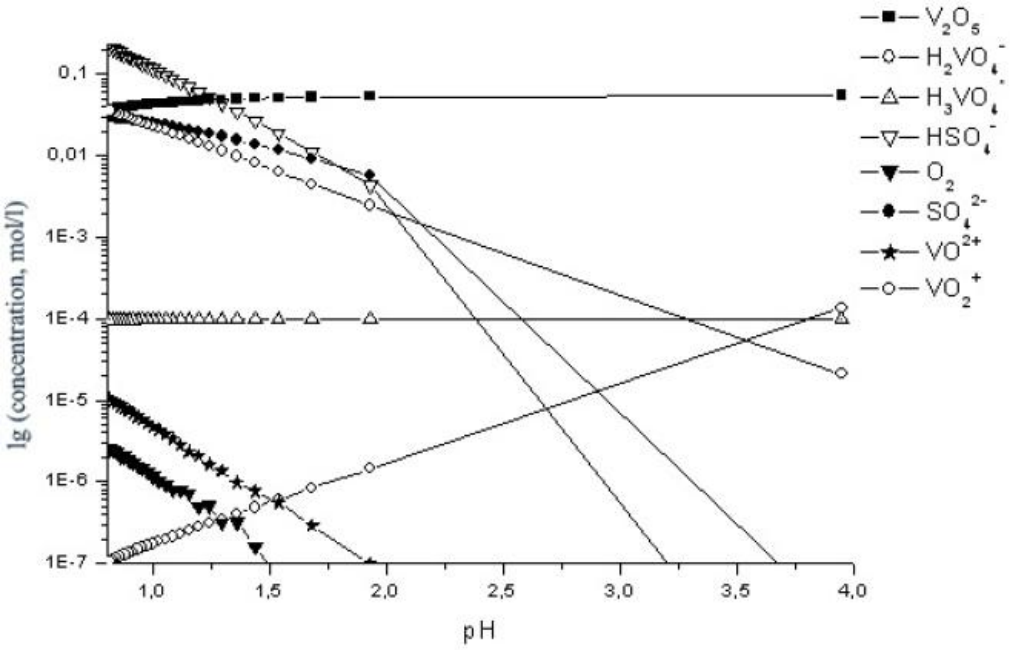

Figure 1.15 Composition of V-O-H-S concentration vs pH [77]

The V-O-H-Na solution consists of 17 phases: V_2O_5,NaOH, $Na_2V_2O_6$, H_3VO_4, VO_2, O_2,H_2, $H_2VO_4^-$, HVO_4^{2-}, $VOOH^+$,VON^{2+},VOH^+, VO^+,VO^{2+},VO_4^{3-},Na^+ as shown in Figure 1.16. Based on this simulation the VO_2 phase is present indicating synthesis of VO_2 in aqueous solution may be possible [77].

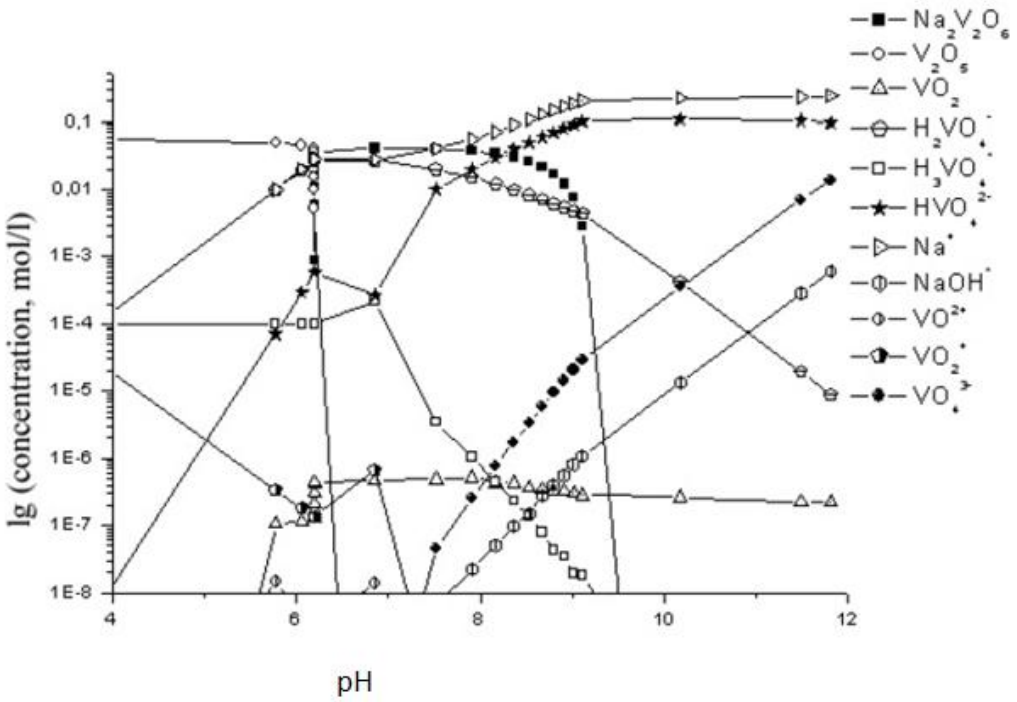

Figure 1.16 Composition of V-O-H-Na concentration vs pH [77]

The computer simulations suggest that VO_2 phase is stable in the solution at pH range from 6 to 11, the highest concentration is found at pH 7.9. Furthermore, the model suggests the particles are found in amorphous form. Further heat treatment is required for crystallization. In addition, dependence of VO_2 on temperature and pressure has also been suggested. That is, in the temperature range from 20 to 100 ℃ the concentration of vanadium dioxide increased as the temperature was raised and VO_2 productions remains constant within a pressure range of 0.1 to 10 MPa [77].

1.2.5 Reduction of V_2O_5 to VO_2

Phase analysis of vanadium oxides by Andersson [64] has revealed eleven discrete oxides phases from VO to V_2O_5; as shown in Appendix 1. The oxides phases from V_2O_3 to VO_2 are Magnêli phases (V_nO_{2n-1}). These phases exist in equilibrium as shown in eq. 3. The existence of mixed phases complicate the production and characterization of vanadium oxide. Their critical temperature are V_3O_5 (157 ℃), V_4O_7 (-23 ℃), V_5O_9 (-138 ℃), V_6O_{11} (-103 ℃), V_7O_{11} (metallic), V_8O_{15} (-203 ℃) and V_9O_{17} (unknown) [78],[64].

$$V_nO_{2n-1} \rightleftharpoons V_2O_3 + (n-2)VO_2 \qquad \text{where } 3 \leq n \leq 9 \qquad (3)$$

At normal temperature and pressure V_2O_5 is thermodynamically the most stable oxide. V_2O_5 can be reduced to lower oxidation state such as VO_2, V_2O_3 or V using reducing agents such as H_2, CO or oxalic acid. Pure V metal can be recovered from V_2O_5 by reducing it with Ca or Mg at a high temperature [79].

Table 1.3 Methods for thermal reduction of V_2O_5 to VO_2 thin films

Annealing material	Annealing parameter	Remark
V_2O_5 + NH_3 and N_2	flow rate –NH_3 (5ml/min) -N_2 (110 ml/min)	for 1 hour at 526 ℃ [80]
V_2O_5 + H_2	T= 200 ℃	for 16 hours [81]
V_2O_5+ H_2+N_2	T= (400-500) ℃, 5 % H_2:95 % N_2	for 3-6 hours [82]
V_2O_5 + H_2O_2	T= 750 ℃ in Vacuum (1.2 x 10^{-4} pa)	for 2 hours, reported lower transition temperature Tc = 62.5 ℃ [83]
V_2O_5 + CO+CO_2	T= 779 ℃ 50 % CO,50 % CO_2	for 30 min, O_2 partial pressure $4x10^{-20}$ atm.[10] [84]

As summarized in Table 1.3, VO_2 can be synthesized from V_2O_5 by reduction using agents such as H_2, CO, NH_3. However, the reduction of higher oxides to a lower oxide has some drawbacks such as increased porosity and surface inhomogeneities due to oxygen escape. As illustrated in Table 1.3, the methods used are for thin films only. Transformation of thin films of V_2O_5 to VO_2 is based on the creation of stability conditions by adjusting the temperature and pressure. The stability conditions can be deduced from the Ellingham diagram of vanadium oxides phase as shown in Figure 1.17. As shown at a particular temperature it is possible to change the phase equilibrium from one form to another [9].

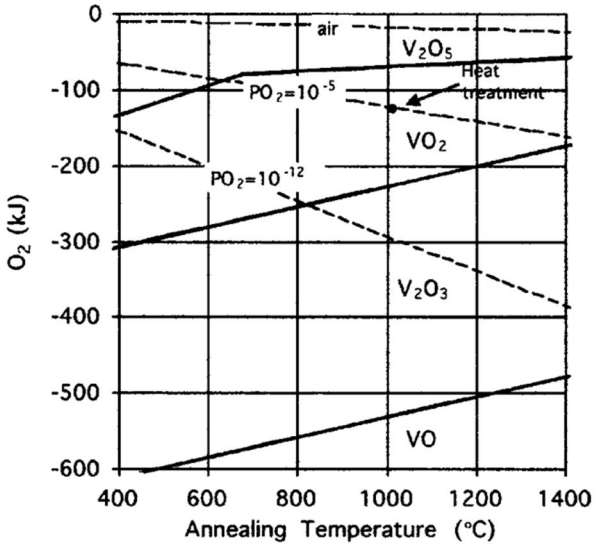

Figure 1.17 Ellingham diagram for vanadium oxide phases, excluding other complex oxides. Figure copyrighted and reprinted from [9], with kind permission from AIP Publishing LLC.

[10] atm = atmospheric pressure (ATM)

V_2O_5 reduction can also be performed by oxalic acid as shown by chemical Eq. (3) [85], [86].

$$V_2O_5+C_2H_2O_4 \rightleftharpoons 2VO_2 + 2CO_2 + H_2O \quad (3)$$

In the synthesis of VO_2 in a liquid phase, it will be helpful to consider vanadium-oxygen partial pressure graph made by Macchesney et al. [84]. As presented in Figure 1.18, the partial pressure of oxygen in liquid phase for solid phase synthesis (VO_2, $VO_{2.17}$) is separated by the solid line. The dot lines represent estimation of possible additional oxides phases. Based on Figure 1.18, it is possible to synthesize (precipitate VO_2) from the liquid phase by controlling the temperature or pressure [84]. A good example is a hydrothermal synthesis method of VO_2 [8], [87-90].

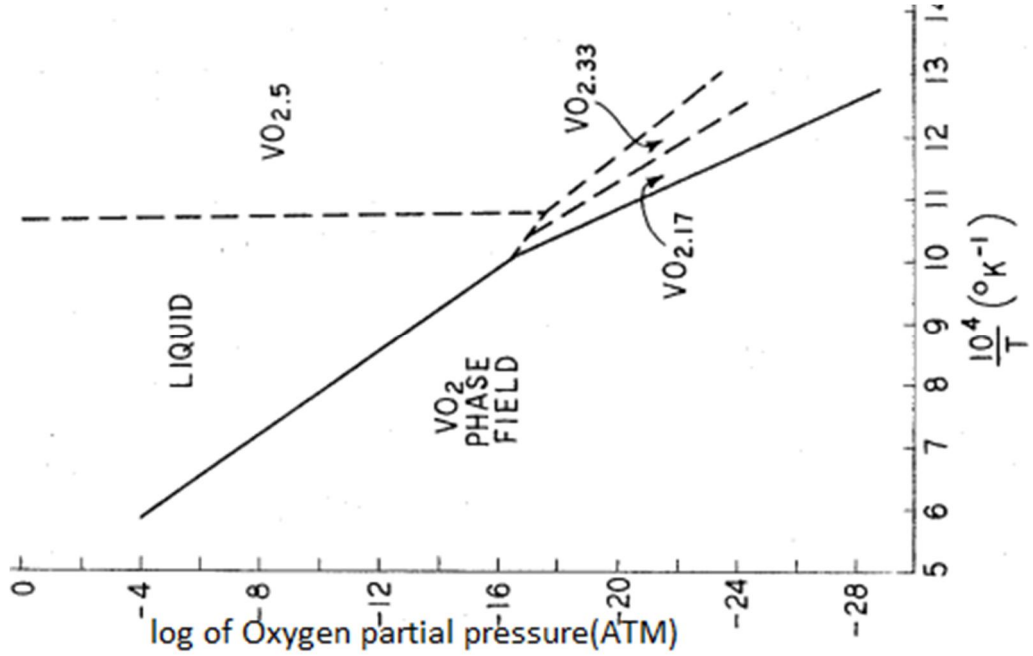

Figure 1.18 Partial pressure vs temperature graph for VO_2 equilibrium phases [84]

1.2.6 Semiconductor to Metal Phase Transition of VO_2

Eight vanadium oxides exhibit a reversible metal to semiconductor transition. The transition is caused by a reversible change in the lattice structural. The same phenomenon is also observed in various transition metal oxides such as Ti_2O_3, Fe_3O_4 and Mo_9O_{26}. In many materials the reversible phase transition can also be triggered by an intense light beam, high electric field or by high pressure. A strong electric field or an incident light beam will trigger a change in the electron density. As the electron density achieves a certain level, the semiconductor phase changes to the metallic phase. According to Crunteanu et al. [91] the phase transition induced by temperature is much slower than phase transition induced by an electric field or a light beam [91], [92].

The metal to semiconductor transition in VO_2 was first discovered by Morin in 1959. Since then, VO_2 has gained attention of various researchers, because its transition temperature is relatively close to the room temperature at 68 ℃ [92]. This characteristic phase transformation particularly in VO_2 and V_2O_3 (T_C= -105 ℃) has many applications for thermally activated optical switching devices [93], [94].

VO_2 phase transition temperature can be lowered by doping with element such as Nb, Mo, Ti, Ta, Ru and W. For instance, phase transition at room temperature can be achieved by doping with 5% W^{6+} [95]. As Manning et al. [96] have reported, doping VO_2 with W lower the transition temperature to 42 ℃ .C.S. Blackman et al. have stated thermochromic properties of VO_2 is tunable between 55 ℃ to -23 ℃ [97]. During doping VO_2 by Mo a transition temperature of 24 ℃ has been achieved as Hanlon et al. have reported [98]. The observed lower transition temperature while doping with high-valent transition metals is due to higher conductivity in the semiconductor state, since the dopant increase the charge carriers. Whereas, doping VO_2 with elements with low-valent such as Cu, Cr, Ge,Ga, Al and Fe increases the transition temperature. There are some drawbacks related to doping, for instance the doping will decrease the transmittance and lower the transmittance difference between the two states [98]. However, this is not always the case; Mlyuka el at. [99] have reported Mg doping increase the transmittance of the visible light.

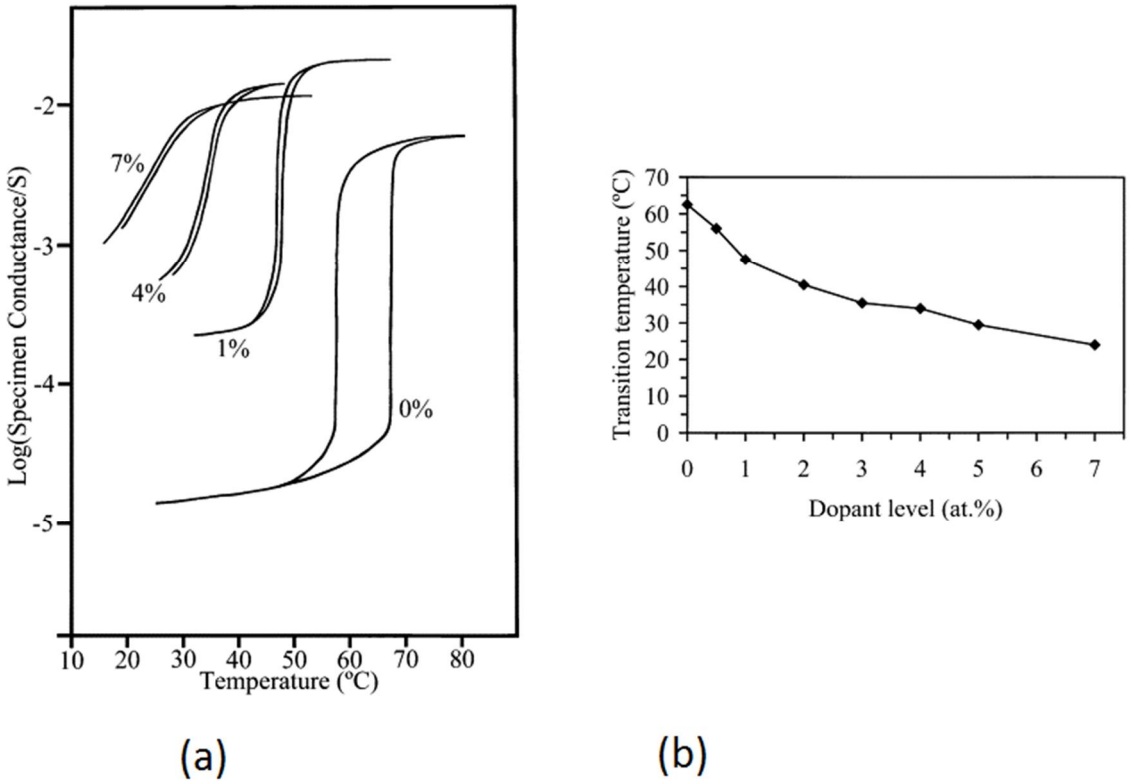

Figure 1.19 (a) Conductance of VO_2 vs temperature, showing the effect of Mo doping percent on the phase transition temperature. The dopant (Mo) narrowed the hysteresis loop from 10 ℃ for undoped to approximately 1℃ for the doped (7%Mo) (b) The transition temperature vs dopant percentage level. Figure copyrighted and reprinted from [98], with kind permission from Elsevier.

The structure of VO_2 in the semiconducting state (at a lower temperature) is monoclinic and in the metallic state (at a higher temperature) it is tetragonal (Rutile) as shown in Figure 1.20. Figure 1.20 (a) shows, the rutile lattice structure of vanadium is arranged in tetragonal body centered unit cell surrounded by six oxygen atoms. The oxygen atoms are arranged in a deformed octahedron. At temperatures below Tc the monoclinic structure is constructed by a combination of two unit cells. The vanadium - vanadium metallic bond is dimerized along the axis. The unit cell enclosing the vanadium dimer is a slanted tetragonal, resulting in a monoclinic unit cell. This slanting causes the octahedron structure of oxygen to be distorted as well [100].

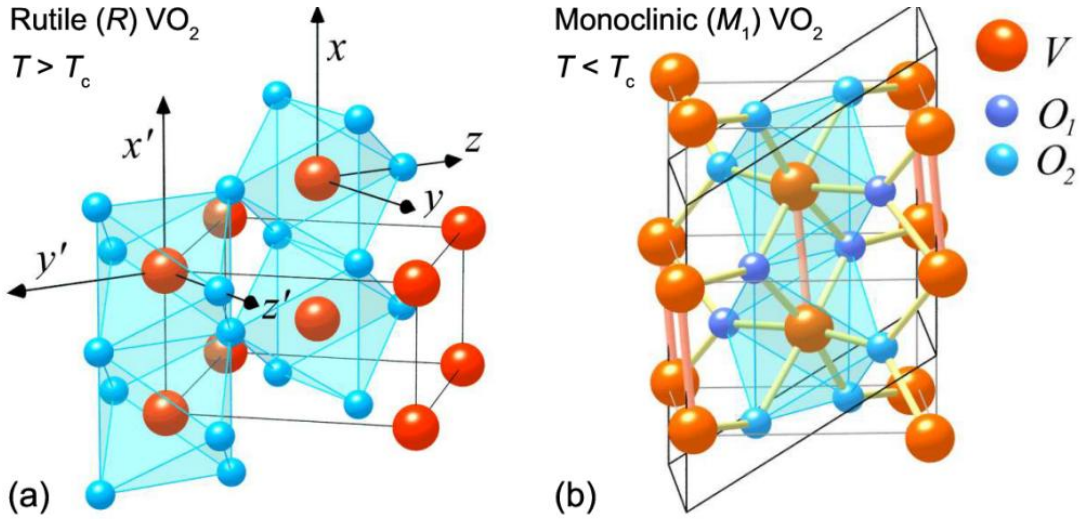

Figure 1.20 Lattice structure of VO_2 (a) Rutile structure above the critical temperature, (b) Monoclinic structure below the critical temperature, exhibiting dimerization of the V-V bonding and zigzag alignment in the vertical direction. Figure copyrighted and reprinted from [101], with kind permission from John Wiley and Sons.

The structural slanting and Columbic interactions are considered the main reason for the semiconductor to metal phase change [100]. The electronic structure of VO_2 is a combination of orbitals of the vanadium atom ([Ar] $4s^2 3d^5$) and the two oxygen atoms ($1s^2 2s^2 2p^4$). The four electrons from V^{4+} will fill the two oxygen atomic orbitals; with only one electron remain in V^{4+} ion. This electron will occupy the d orbital near the Fermi level ($3d^{\prime}$). The 2p electrons of oxygen have no contribution to the electrical conductivity. Since, the electron orbital is well below the Fermi level. The d orbitals of the vanadium ions split into lower energy t_{2g} and e_g^{σ} orbitals. e_g^{σ} Orbital remains unoccupied due to its higher energy state while the t_{2g} orbital is further split into bonding (a_{1g}) and antibonding (e_g^{π}) orbitals. Then, one electron of V^{4+} will occupy a_{1g} orbital. Therefore, based on the arrangement of V-V and oxygen the band gap of a_{1g} and e_g^{π} differs [102].

The zig zag alignments, of V-V bonding, in monoclinic lattice structure, occur in c-axis direction. This alignment also affects the octahedral structure of oxygen to slant. These rearrangements raise the energy of the e_g^{π} orbital higher, thus monoclinic behaves

as a semiconductor. In the rutile structure the a_{1g} orbital is aligned towards the c-axis leading to metallic behavior [102]. The reversible phase transition is further explained thermodynamically in section 1.2.7 (Thermodynamics of the Phase Transition).

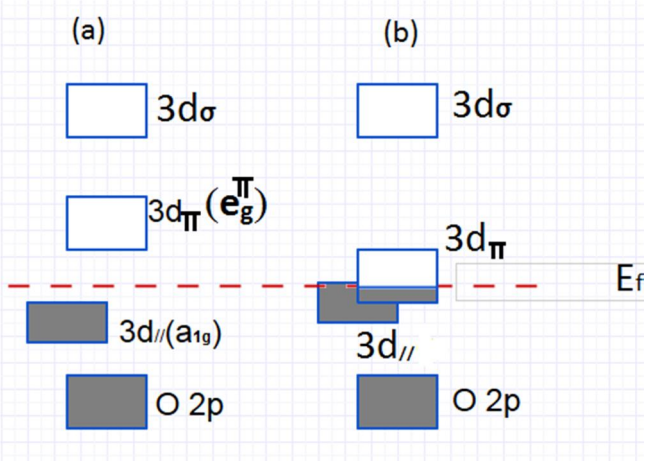

Figure 1.21 (a) Monoclinic structure with wider band gap of a_{1g} and e_g^{π} (b) Rutile structure which behaves as a metal (the figure slightly modified from [103])

1.2.7 Thermodynamics of the Phase Transition

The phase transition in VO_2 is driven by the reduction of total free energy of a system. As shown in Figure 1.22, the free energy of the metal and semiconductor phases follows different free energy paths. At the critical temperature, the two forms equilibrium at the intersection of the curves (G_{metal} and G_{smi}). The lower energy path of the free energy for the system is represented by dot lines in the figure [3].

$$G = H - TS \qquad (4)$$

Where G is the total free energy, H is the enthalpy and S is the entropy

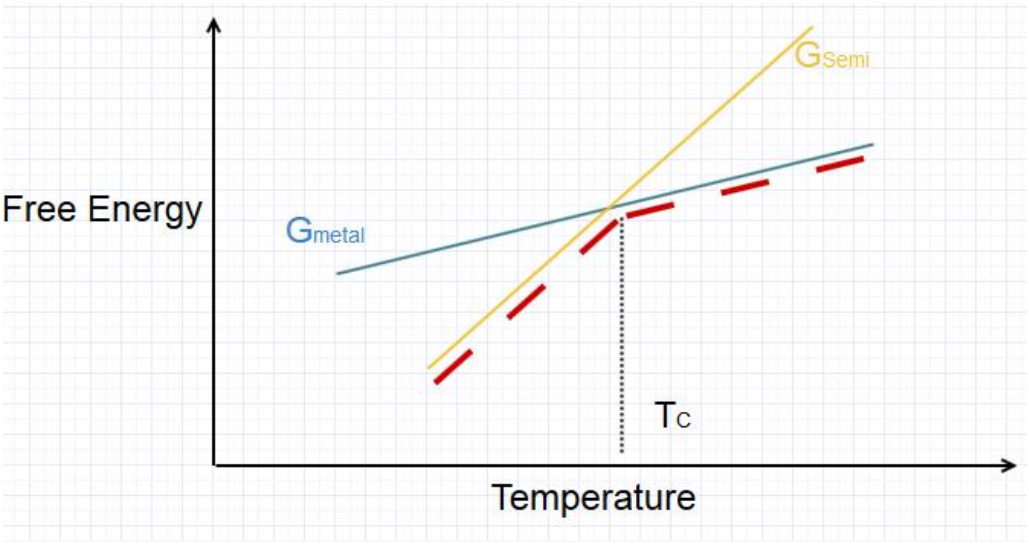

Figure 1.22 The free energy of the VO_2 system drives the transition from G_{metal} (methal phase) to G_{semi} (semiconductor phase), figure slightly modified from [3])

At critical temperature (T_C) the conductivity of VO_2 changes by 4-5 orders of magnitude. That is the conduction band gap is more than KTc at a temperature less than Tc the material act as an insulator. The electron concentration in the metallic phase is in the order of 10^{21} cm^{-3} (i.e typical of metal). Therefore, at a temperature greater than T_c the oxide acts as a conductor due to increase in electron density (band gap less than KT_c). During the temperature increment, there will be excitation of electrons resulting in the exponential increment of resistivity (increment of electron density), which then leads to metallic phase [104], [105].

Furthermore, based on John Rozen [106] explanation, the synthesis of VO_2 usually introduces impurities, making VO_2 n-type semiconductor. Conductivity (σ) is directly proportional to electron concentration [106].

$$\boldsymbol{\sigma = nq\mu_n} \tag{5}$$

Where n= electrons concentration, q= charge of electron, μ= carrier mobility
The exponential relation of temperature and electron concentration is derived as follows

$$n(T) = \mathbf{N_c exp}\left(\frac{\mathbf{E_f - E_c}}{\mathbf{KT}}\right) \tag{6}$$

Where N_c = effective density, E_f= energy of the Fermi level, E_c= lowest energy of the conduction band and K= is the Boltzmann constant. Therefore, the conductivity is expressed by replacing energy of the band gap with activation energy E_a and introducing pre-exponential factor σ_0

$$\boldsymbol{\sigma(T) = \sigma_0 exp}(-\frac{\mathbf{E_a}}{\mathbf{KT}}) \tag{7}$$

The transition of electrons are also explained by models such Peierls transition and Mott-Hubbard transition. However, none of these models completely explained the phenomena observed in the phase change. Several studies have been done to understand the conductivity change, but there is no unifying explanation. The two widely presented explanation the Peierls mechanisms, which describes structural vanadium-vanadium dimerization or separation and the Mott Hubard transition, which describes an electron-electron interaction lack to describe the phenomena [106], [107].

Similarly, the transition affects the optical properties of the oxide. Especially, near infrared region transmittance of metallic phase is less than semiconductor phase. This is due to the absorption of wavelength greater than 600 nm by the metallic phase. The monoclinic phase is transparent in infrared, radio and microwave frequencies. This optical transmittance change caused by temperature change can be used in “smart windows” such as cars and building [106], [108].

1.3 Electrophoretic Deposition

Electrophoretic deposition (EPD) is a solvent based process for deposition of particles by a direct current (DC) between electrodes. Electrophoretic deposition differs from electroplating. Electroplating is a deposition mechanism of ions by reduction in conductive solvent. EPD is used for suspended particles in a low conductivity solvent; usually

organic solvent. EPD was discovered by Ruess, a Russian scientist, in 1808. Since then, EPD has gained popularity for its numerous advantages such as for its low cost, fast production rate, suitability for coating of objects of various shapes. The drawback of EPD, it is not used in water based solvent due to the dissociation of water into oxygen and hydrogen by the applied electric current. These gases and presence of ions will adversely affect the coating quality. The main mechanism of EPD is mobility of charged particles under the influence of an electric field. Hence, depending on which electrode the deposition occurs, EPD can be classified as cathodic EPD or anodic EPD [109].

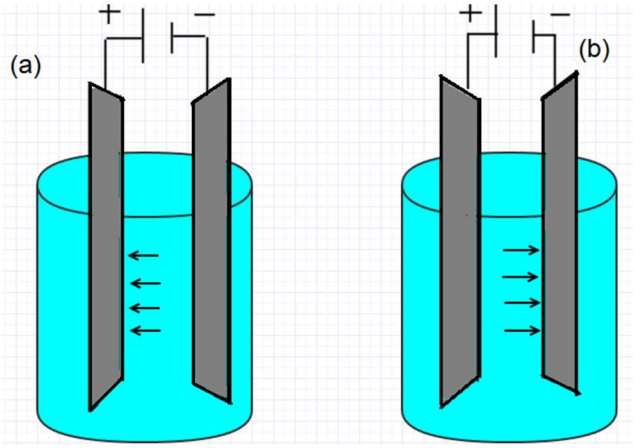

Figure 1.23 EPD schematic diagram (a) Anodic type EPD (b) Cathodic type EPD

1.3.1 Factors influencing EPD

EPD is influenced by the properties of the solvent, the suspended particles in the solvent, electrical conductivity of the electrodes and the applied electric field. These parameters are quantitatively expressed by Hamaker's law and Avgustinik's law as shown in eq. 4 and 5 respectively. The Hamaker's law determines the deposited mass (m) in terms of the electrophoretic mobility μ, the strength of the electric field (E), the electrode surface area (a), the concentration of the particles (C). Avgustinik's law estimates the mass from the length of electrode (l), the permittivity of the solvent (ε), the zeta potential of the particles (ζ), the deposition time (t), the radius of the electrodes r_1, and r_2 and the viscosity of the solvent (η) [109].

$$\mathbf{m} = \int_{t_1}^{t_2} \boldsymbol{\mu} \cdot \mathbf{E} \cdot \mathbf{a} \cdot \mathbf{C} \cdot \mathbf{dt} \quad \text{(Hamaker's law)} \tag{4}$$

$$\mathbf{m} = \frac{\mathbf{l} \cdot \mathbf{E} \cdot \boldsymbol{\varepsilon} \cdot \boldsymbol{\zeta} \cdot \mathbf{C} \cdot \mathbf{t}}{\mathbf{3} \ln\left(r_1/r_2\right) \cdot \boldsymbol{\eta}} \quad \text{(Avgustinik's law)} \tag{5}$$

As quantitatively expressed by Hamaker's and Avgustinik's laws there are numerous factors which influence EPD. Those related to the particles, those related to the solvent and those related to working condition. The variables can be categorized in groups for instance factors related to the particles are conductivity, zeta potential, and

stability of the suspension. Factors related to the experimental setup are deposition time, applied voltage, concentration, conductivity and shape of the electrodes [109].

High quality EPD can be achieved if the particles are dispersed uniformly throughout the liquid. The dispersion of particles improves as their size decreases, since larger particles have a tendency to sediment. Thus, depositions can be thicker at the bottom and thinner at the top of the electrode. Furthermore, during drying deposition of larger particles tend to crack more than those made from smaller particles [109].

Extremely high stability of the suspension due to intermolecular attraction between the liquid and the particles can lead to less mobility of particles which restricts deposition. To some extent the suspension has to be less stable in the vicinity of the electrodes. To determine condition for deposition zeta potential or electrophoretic mobility helps. For instance, dense deposition is achieved when the particles have high zeta potential. Better deposition and rate is achieved by increasing zeta potential, for instance by varying the pH of the solution. However, additive which influence the zeta potential can also change the conductivity of the solution. If conductivity is high particles mobility is less, and if conductivity is less then particles sediment losing charge. Therefore, non-aqueous liquids with low dielectric constant, low viscosity and low conductivity are preferred [109].

Other factors which affect EPD are related to the working parameters. Increasing applied voltage or shortening the distance of the electrodes increases the electric field and will increase deposited amount. However, better quality is achieved at moderate electric fields (25-100 V/cm). A high electric fields (>100 V/cm) leads to a high deposition rates and often leads to non-uniform deposition. Furthermore, higher electric fields may generate turbulence in the suspension which will affect the quality of the deposition. During constant electric fields, a longer time parameter will decrease deposition. That is, initially the deposition increases linearly but during a long process it will decrease. This is because of electrode insulation (coated) as deposition progress [109].

The conductivity of the electrode is also critical for both the deposition rate and the quality. For example, a less conductive electrode result non-uniform deposition and slow rate of deposition [109].

1.4 Characterization Techniques

This topic deals with the main characterization techniques used in this thesis, namely scanning electron microscopy (SEM), Transmission electron microscopy (TEM), optical spectroscopy and Raman spectroscopy.

1.4.1 Scanning Electron Microscopy (SEM)

The word microscope is derived from the Greek words mikros (small) and skopeo (look at). A microscope is used to see objects that are too small to be seen by the naked eye. Human eye can see objects with a resolution of approximately 0.1 mm at a distance of 25 cm, whereas the best optical microscopes have a resolution of 200 nm. Resolution is

defined as the minimum distance at which two objects can be distinguished. Optical microscope resolution has been improved to electron microscope by replacing light source with high energy electron beam. The resolution that can be achieved by electron microscopes is 0.05 nm for TEM and less than 0.5 nm for SEM [110], [111].

SEM technique produce data of topographic images and compositional information during interaction of electron beam with the specimen. The interaction produce back scattered, Auger and secondary electrons as shown in Figure 1.24 [111]. The most commonly used signals in SEM are back scattered and secondary electrons.

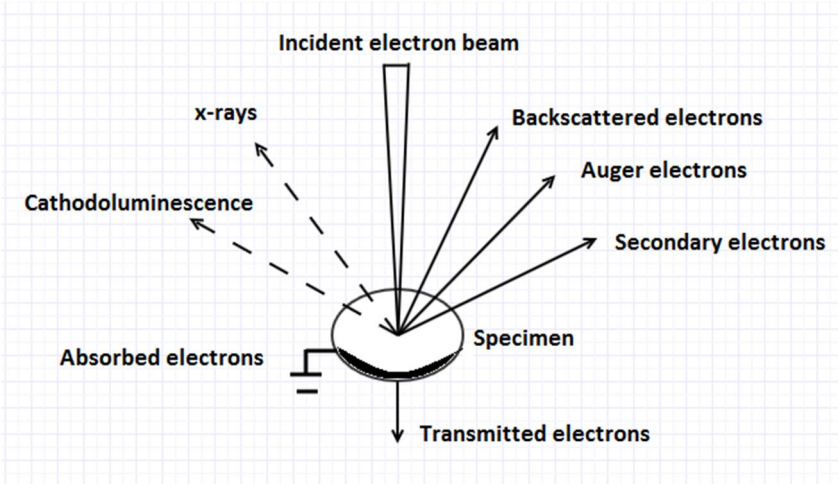

Figure 1.24 Signals produced by interaction of the electron beam with the specimen consist of secondary electrons (SE), back scattered electrons (BSE), Auger electrons, x-rays and cathodoluminescence(CL).

Back scattered electrons originate from the beam and they are elastically scattered from the sample. The backscattered electrons signal differ based on beam energy, atomic number and density. As atomic number and density increase the scattering also increase. Thus, during backscattering images areas with higher atomic number elements appear brighter and smaller atomic number elements as darker areas. Therefore, backscattering imaging is useful for estimating the compositional distribution. The backscattered electrons signal depends also on the roughness of the surface [111].

Secondary electrons (SE) are produced by the incident electron beam colliding with the electrons of the atoms of the sample. Secondary electrons have typically low energy below 50 ev. As a result, only electrons from the top surface from the thickness of 5 nm escape while electrons from deeper depth do not have enough energy to escape. This makes SE surface sensitive. To generate signal, SE will be attracted by the detector (Evehart Thornley detector). Then, it will be converted to a photon by a scintillator. Next, the photon signal will be amplified by a photomultiplier and after amplification photon will be converted back to electrons. The electrons current (as signal) is used to form images contrast on the screen. Stronger signals produce bright areas and weaker signals form darker areas in the images [110-112].

For an SEM analysis a sample must be conductive. Insulator samples are coated by carbon or a metal using either ion sputtering or vacuum evaporation technique. Coat-

ing by a conductive layer prevents charging of the sample, minimize thermal damage and enhance the SE electrons signals [112] .

1.4.2 Transmission Electron Microscopy (TEM)

Transmission electron microscope (TEM) is a vital instrument for characterization of nanomaterials. Similar to SEM, TEM uses an electron beam for the characterization. In TEM a very thin sample is used which is partially transparent to the electron beam. The transmitted electrons are used for imaging. In terms of magnification and resolution TEM is superior to SEM. SEM is helpful for capturing a three dimensional image with better depth of field. TEM images are two dimensional and the whole image is taken at one time [113], [114].

Sample preparation for TEM can be challenging for thick solid materials to make them electron transparent. Sample preparations include grinding, polishing and milling. For instance, at a voltage of 170 kV a thickness below 60 nm is needed. In some special cases (for nanoparticles insolvents) simple spreading and drying of the solvent on a thin holey carbon support film is sufficient [113], [114].

In TEM secondary backscattered electrons can also be used. However, the spatial resolution is much better for the transmitted electrons. Transmitted electron detectors are classified as bright field or dark field detectors. In bright field detector, transmitted beam and holes create bright images while in dark field detectors transmitted beam and holes create dark images. These detectors provide complementary information [114].

1.4.3 Optical Spectroscopy

Electromagnetic radiation used for optical spectroscopy consists of ultraviolet (UV, 200 nm- 400 nm), Visible (VIS, 400-780 nm) and near infrared (NIR, 780-2500 nm) wavelength regions. When an electromagnetic wave interacts with matter, some of the energy is reflected back, some is transmitted and some scattered. This interaction of light with matter is used to study properties of matter, for instance composition [115].

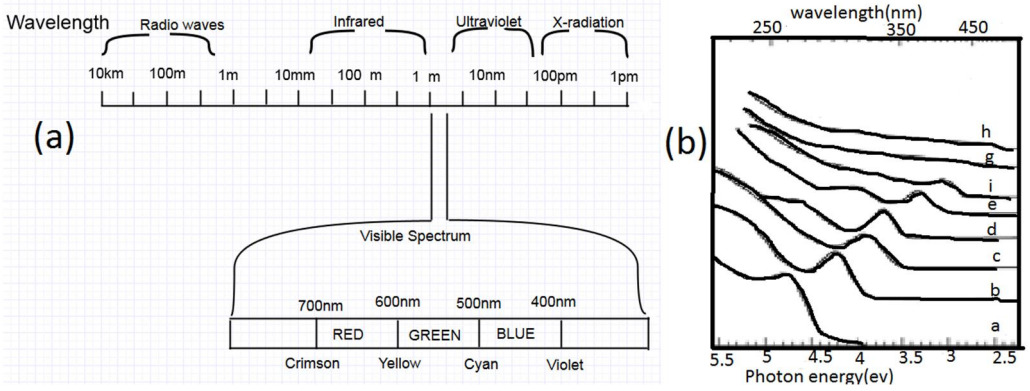

Figure 1.25 (a) Bands of the electromagnetic spectrum (figure slightly modified from [115])(b)UV-Vis spectra vs absorption coefficient of CdS nanoparticles with increasing nanoparticles size from a-h (a=6.4Å, b=7.2Å,c=8Å, d= 9.3Å,e=11.6 Å, f=19.4Å, g=28Å, h=48Å)(figure slightly modified from [116])

Optical absorption spectroscopy compares intensity difference between incidents (I_o) and transmitted (I) light by using the Beer-Lambert law. Based on the Beer-Lambert law, transmittance T, molar absorptivity ε, optical path length L, concentration C, are related as shown in eq. (6-8). Usually, the absorption is plotted as a function of the wavelength [115].

$$\boldsymbol{I = I_O \exp(-\varepsilon C L)} \quad (8)$$

$$\boldsymbol{T = \frac{I}{I_O} = \exp(-\varepsilon C L)} \quad (7)$$

$$\boldsymbol{A = log \frac{I_o}{I} = \varepsilon C L} \quad (9)$$

Optical spectroscopy can be used to determine color of the materials, photoluminescence, photovoltaic, photocatalytic and photoelectrochemical properties [115]. As shown in Figure 1.25 (b) UV-Vis absorption spectra can also be used to monitor nanoparticles relative size changes. The absorption peak as can be seen in Figure 1.25 (b) blue shifted for smaller nanoparticles.

1.4.4 Raman Spectroscopy

Raman spectroscopy is used to study vibrational, rotational and low frequency modes of a system based on Raman scattering of monochromatic light; such as laser. Some of the laser sources used are Ar^+ (351-514.5 nm), Kr^+(337.4-676.4 nm) and Nd-YAG laser (1,064 nm). In Raman spectroscopy sample irradiation by monochromatic light cause scattering of light as Rayleigh scattering, this is intense elastic scattering. Very few photons, approximately in the range of one in a million, of the incident beam (V_O) scatters inelastically with a Raman shifted wavelength [117-119].

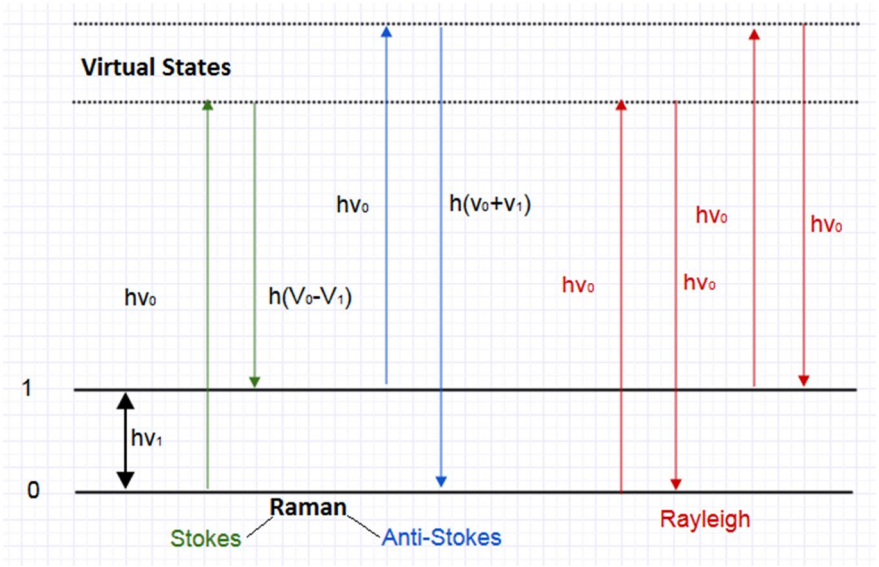

Figure 1.26 Raman and Rayleigh scattering

Raman Effect is a shift in frequency (ΔV) which takes place during excitation of a molecule and de-excitation as shown in the Figure 1.26. The shift in frequency occurs because of energy difference between the initial excitation and the final de-excitation

state. The Raman frequency may increase ($v_o + v_m$) which is called an anti-Stokes shift or when it decrease ($v_o - v_m$) is called a Stokes shift. In Rayleigh scattering the excited molecule after relaxation return back to the initial level without a shift in frequency of light. Raman shifts provide information about the sample. Typically the interesting Raman shifts are observed in the wavenumber range from 10^2-10^4 [117-119].

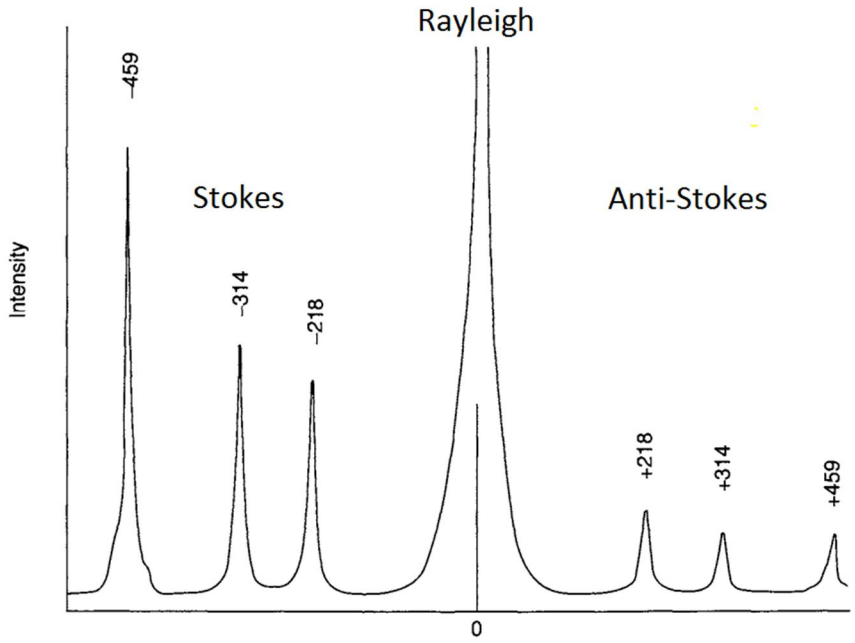

Figure 1.27 CCl_4 Raman spectrum, the highest signal represent Rayleigh and the least intense signal represent anti Stokes shifts. The intensity of the Stokes shifts is higher than anti-Stokes shifts. Figure copyrighted and reprinted from [117], with kind permission from Elsevier.

Rayleigh scattering is about 99.999 % of the incident beam, which have no significant information for characterization. Thus, to improve Raman signal ($v_o \pm v_m$), which is 0.001 % of the incident beam, a unique filtration techniques such as notch filters, tunable filters, laser stop apertures, double and triple spectrometric techniques are used [118].

Approaches based on filters are limited to detection of Raman shifts larger than 100 cm^{-1}. Double and triple spectrometers can be used to detect Raman shifts as low as 3-5 cm^{-1}. Typical Raman spectroscopy constitutes of the following major instrumental parts the laser, wavelength selector (filter, spectrophotometer), detector (photodiode array, CCD, PMT). Simple single grating based Raman monochromator schematic diagram is shown in Figure 1.28 [118].

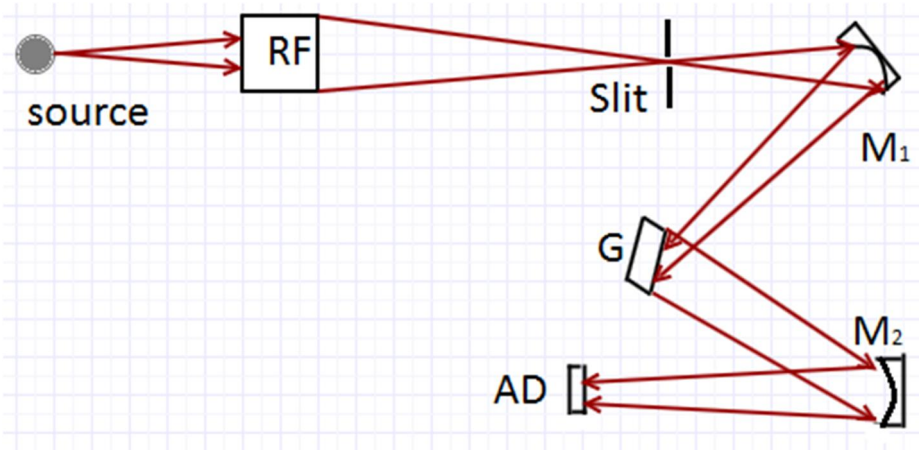

Figure 1.28 Schematic diagram of single grating based Raman system. The scattered light incident on RF (Rayleigh filter) to separate Rayleigh scattering, G(grating), M_1 and M_2 are spherical mirrors, AD(array detector). The figure is slightly modified from [120].

The weak Raman signals require high sensitivity detection systems and careful optimization of the optical setup. Further, fluorescences from impurities also pose challenge which might sometimes dominate the Raman signal. In addition, metals are not Raman active. In spite of these drawbacks, Raman offers various advantages. For example, solid and liquid samples can be characterized, there is no unique sample preparation, it is a nondestructive method, it can be used to characterize a small volume (less than one μm in diameter), and measurement is fast. A Raman spectrum is a fingerprint of the sample that can be easily compared with a standard, which simplify characterization process [121].

2. EXPERIMENTAL PART

This chapter discusses techniques used in the PLAL experiments for fabricating vanadium oxide and metallic vanadium nanoparticles. The experimental part is divided into sections based on the solvent used. Each section contains the description of methods, results of the experiments and discussion of the results.

The experiment was carried out using a high repetition rate fiber laser ($\lambda \approx 1060$ nm, pulse width 20 ps, repetition rate 1MHz, average power of 1.1 W, peak power 55 KW, FWHM of the focused beam ≈ 15 µm). The ablation was carried out in 3.5 ml acrylic cuvette or quartz cuvette based on the liquid type. The acrylic cuvette was used only for water and water + SDS.

In the experiments, due to high reactivity of vanadium different liquids were used; liquids such as acetone, mixture of acetone and H_2O, acetonitrile, ethanol, deionized water (DI water), mixture of DI- water and SDS, methanol, hydrogen peroxide and 2-propanol. To measure liquids volume mechanical pipette or a syringe is used. Vanadium target used in the experiments was 99.8 % pure.

The experimental setup is similar to the arrangement discussed in the theoretical section, as shown in Figure 1.1 b. In this experiment, the target is suspended using a plate holder as shown in Figure 2.1, which will be fixed on adjustable cuvette holder. Figure 2.2 shows a schematic diagram of PLAL setup used in the experiments.

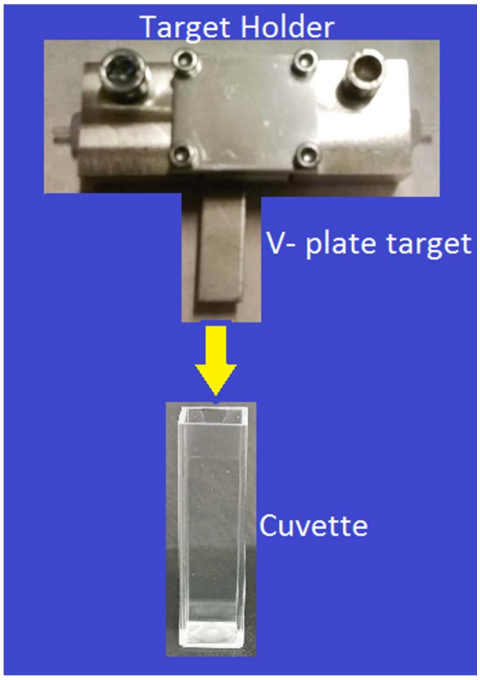

Figure 2.1 Target holder, which is used to hang the vanadium plate inside the cuvette.

During ablation the laser beam is scanned over the target with a 2D mirror scanner to minimize crater formation and to reduce overlap of laser pulses. The scanning speed was 2 m/s.

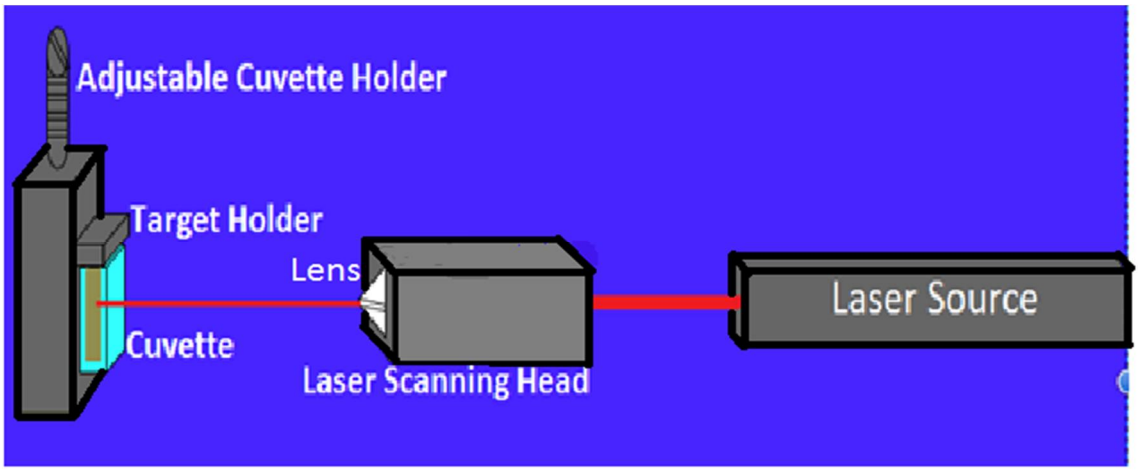

Figure 2.2 Schematic diagram of PLAL set up used in the experiment

2.1 PLAL for Production of Vanadium Nanoparticles

Synthesis of less noble transition metallic nanoparticles which are stable in a solvent for a long period of time is challenging for many techniques; for example chemical synthesis method. The chemical method uses stabilizers to protect the particles from agglomeration and unwanted reactions. In addition, the chemical method uses a combination of different chemicals to achieve the production of desired nanoparticles. The various chemicals increase the amount of impurities in the nanoparticles as reporter by Miyachi et al. [122].

This experimental section presents a one-step synthesis of vanadium nanoparticles by PLAL. Depending on the solvent the produced nanoparticles are stable from weeks to months. To investigating the relative stability of the nanoparticles the following solvents were used: acetone, acetonitrile, pyridine, ethanol, 2-propanol and DI water (with SDS as a stabilizer). PLAL of vanadium in these liquids was carried out for 10-20 min.

2.1.1 PLAL in DI-Water and SDS

Vanadium nanoparticles generated in water by PLAL are not stable (this will be discussed further in section 2.2.2). SDS was used to stabilize vanadium nanoparticles in water. SDS is an ionic surfactant. It stabilizes vanadium nanoparticles in DI-water by creating a water repealing layer. SDS has hydrophilic head and hydrophobic tail as shown in Figure 2.3 (a). The hydrophilic head attaches itself on the surface of vanadium, while the hydrophobic tail is directed out ward creating a repellant layer as shown in Figure 2.3 (c). The presence of SDS in the solvent will minimize the interaction of water with the metal surface, thus slowing down the rate of oxidation and solubility.

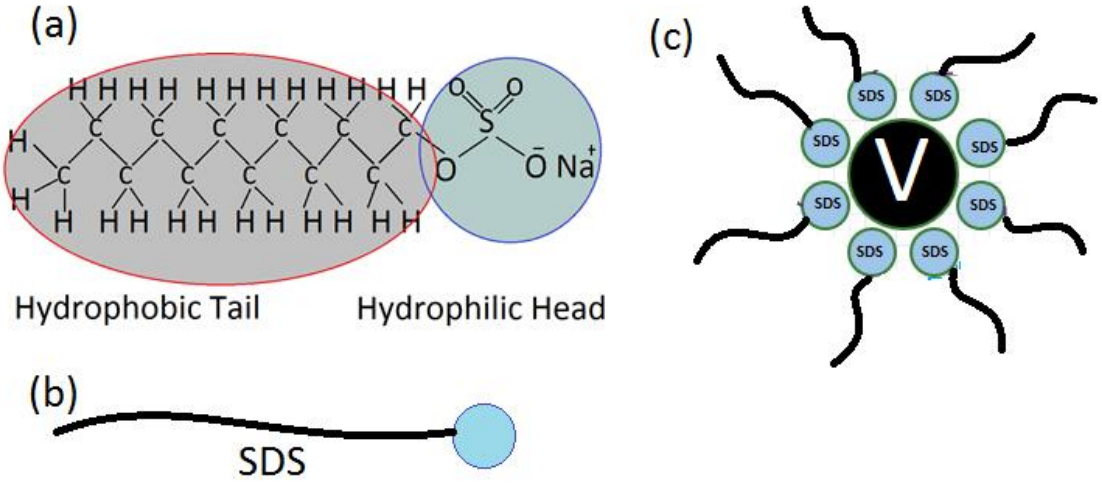

Figure 2.3 (a) Structural representation of sodium dodecyl sulfate (SDS) $NaC_{12}H_{25}SO_4$, (b) Representation of SDS with a tail and head (c) Schematic representation of SDS as a protecting layer, where the hydrophilic head attaches on the surface of vanadium and the hydrophobic tail creates a shielding from water.

SDS as stabilizer for vanadium nanoparticles was investigated with concentrations of 10, 1, 0.5,0.1, and 0.01 mM. The ablation was carried out for 10 min by following the same procedure as presented in the introduction section of this chapter. After ablation, the sample was transferred in to an air tight container (snap seal vial). The observed initial color of the liquid just after ablation is in the range of dark to light gray based on the concentration of the ablated particles. High concentration of ablated particles produced dark gray solutions. The SDS concentration influenced the production rate of the nanoparticles. As the concentration of SDS was increased the color of the sample became light gray indicating less production rate of vanadium nanoparticles. The lower ablation rate is a result of SDS tendency to produce gas bubbles in the liquid and on the target surface. As a result, laser light will be scattered before reaching the target surface, and the effective laser power is reduced.

After a day, the samples with SDS concentration below 0.5 mM changed from the initial light gray to colorless. Solutions with concentration higher than 0.5 mM of SDS slowed the rate of reaction for a week. After a week, the gray color gradually changed to colorless.

After 15 min of ablation, a sample was prepared on silicon substrate by drop cast method from 0.5 mM of SDS for SEM analysis and for another SEM sample after 20 hours. As shown in Figure 2.4 and from visual observation, SDS concentrations above 0.5 mM preserved the particles for one week.

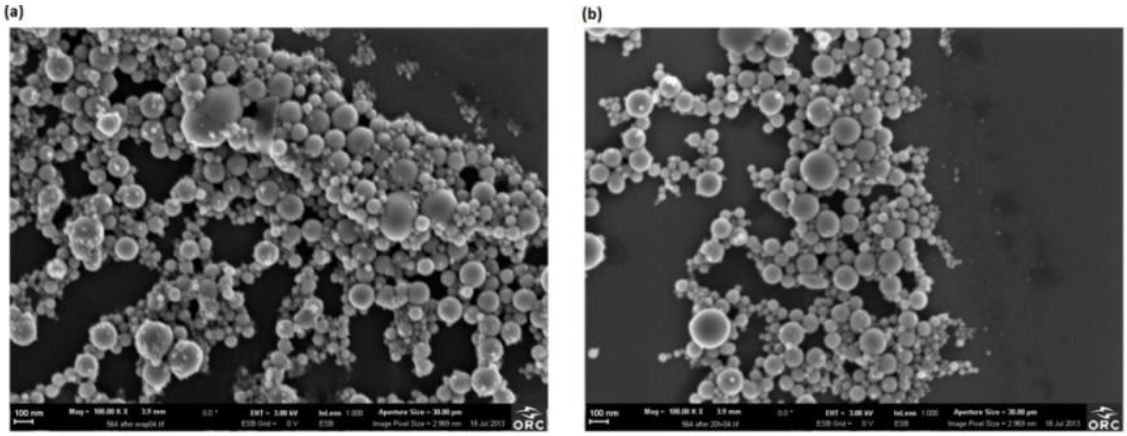

Figure 2.4 (a) SEM image taken after 15 min of PLAL from 0.5 mM of SDS sample (b) SEM image taken after 20 hours from the same sample. Vanadium nanoparticles were stable in 0.5 mM for one week.

2.1.2 PLAL in Organic Solvents

Organic solvents used in the experiments were ethanol, 2-propanol, acetone, acetonitrile and pyridine. These solvent are classified in two categories: polar protic solvents and polar aprotic solvents. Solvents such as ethanol and 2-propanol are classified as polar protic while solvents such as acetone, pyridine and acetonitrile are classified as polar aprotic solvent.

It was found vanadium nanoparticles are stable in polar aprotic solvents (acetone, pyridine and acetonitrile) for more than a month. The color or the samples after ablation in these solvents is dark gray indicating high production rate. In the case of polar protic solvents (ethanol and 2-propanol), the particles were stable for one month only. The color changed from dark gray to colorless slowly after a month of aging indicating slow oxidation reaction.

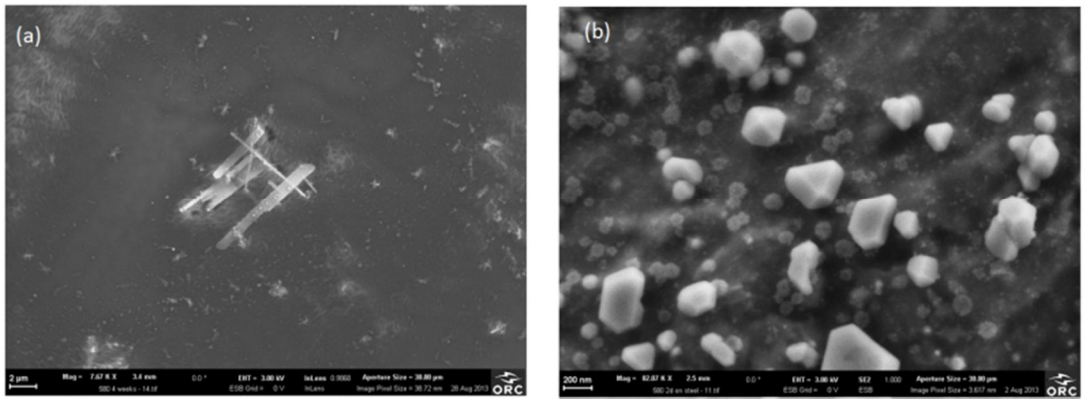

Figure 2.5 (a) Particles formed after a month of aging in ethanol, (b) Particles formed after two days of aging in 3.2ml of ethanol and 0.3ml of DI-water mixture. Because of further reactions the particles were not stable in ethanol.

Vanadium nanoparticles in alcohol showed oxidation due to the presence of water. Thus, by increasing the amount of water by a small portion (approximately 8 % i.e

0.3 ml H_2O and 3.2 ml of ethanol) it was possible to increase the rate of oxidation and nanoparticles with lower stability were formed as shown in Figure 2.5.

2.2 PLAL for Production of Vanadium Oxide in Di-Water

PLAL was carried out in DI-water to study direct production of vanadium oxide. Before ablation, the weight of the target was $(72454\pm3)*10^{-5}$ g. After 10 minutes of ablation the weight of the target had lowered by $(13\pm4)*10^{-5}$ g. The rate of production in this experiment was $(1.0\pm0.4)*10^{-5}$ g/min.

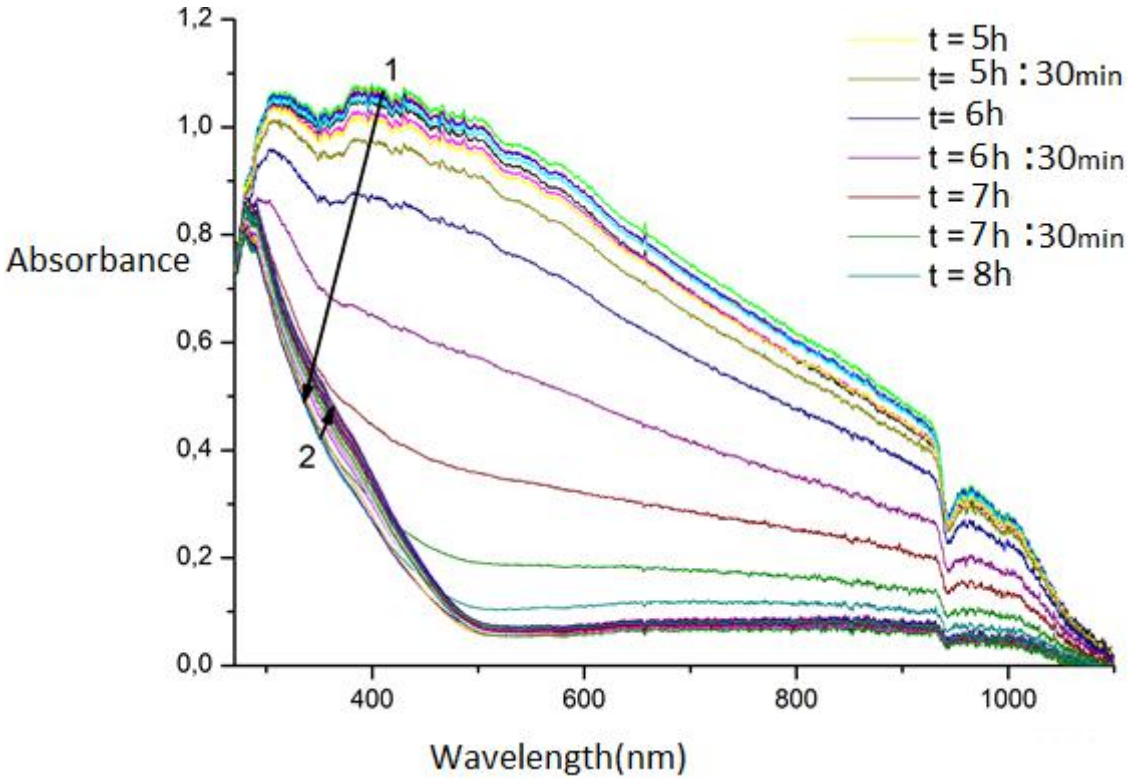

Figure 2.6 Development of the absorption during 12 hours following the preparation of the sample in DI-water. Each individual spectrum measurement shows change within 30 minutes intervals. Arrow 1 indicates the changes during the first 7 hours. In the first 4 hours the change is slow and after $4\frac{1}{2}$ hours the change is pronounced. Arrow 2 indicates changes after the nanoparticles have dissolved and the increase toward a stable state.

After ablation, the sample was kept in an open acrylic cuvette to monitor the changes in the optical spectra for 12 hours and the resulting spectra are shown in Figure 2.6. The initial measurement shows a broad beak at around 450 nm which is absorption peak of vanadium nanoparticles. Slowly, the absorption peak deceased to lower wavelength as shown by arrow 1, and each individual spectrum is taken within a 30 min interval. After 7 hours the broad absorption peak has disappeared. This slow disappearance of the peak is related to conversion of vanadium nanoparticles in to ions. As the optical spectroscopy shows the main reaction takes within 4-6 hours. The color of the

solution changed from gray to light yellow which might indicate formation of $[VO_2(H_2O)_4]^+$ ions. The SEM image as shown in Figure 2.7 also shows non-existence of nanoparticles.

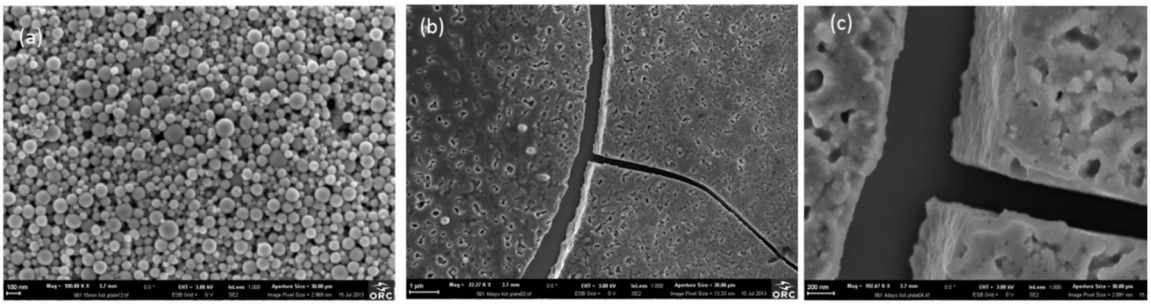

Figure 2.7 (a) SEM image after 15min of ablation indicates the presence of vanadium nanoparticles, (b) and (c) SEM image taken after 4 days of aging indicates the vanadium nanoparticles have dissolved in DI-water.

The samples were studied by Raman spectroscopy withing 4-5 hours of aging. The Raman spectrum indicates presence of V_2O_3. To support the experimental findings the result was compared to the thermodynamics of V-H_2O at 25℃ by Kelshall et al. [123] and as shown in Figure 2.8, the red line indicates vanadium concentration achieved by PLAL in this experiment.

$$\log(V) = -log\left[\frac{moles\ of\ the\ solute}{liters\ of\ the\ solution}\right] = -\log(0.0007) = 3$$

$$(Where, moles\ of\ the\ solute = \frac{mass\ of\ the\ substance}{molar\ mass} = \frac{0.000127g}{50.94\ {}^{g}/_{mol}}$$
$$and\ liters\ of\ the\ solution = 0.0035\ L)$$

According to Kelshall et al. VO and V_2O_3 could exist at neutral pH, with V_2O_3 as the dominating oxide. Possibility of synthesizing V_2O_3 by controlling the aging time needs further investigation. Based on Figure 2.8 (c) and Figure 1.13, VO_2 and V_2O_5 are challenging to synthesize within this production rate and pH. For production of the most stable oxide (V_2O_5) the concentration should be nearly 20 times higher than the production of this work and additional pH adjustment is needed. For VO_2 synthesis, the optimal pH value is 5 as shown in Figure 2.8 (c). However, because of the lower stability of VO_2 (like VO and V_2O_3) it will most probably not stable, at least in a water based solvent.

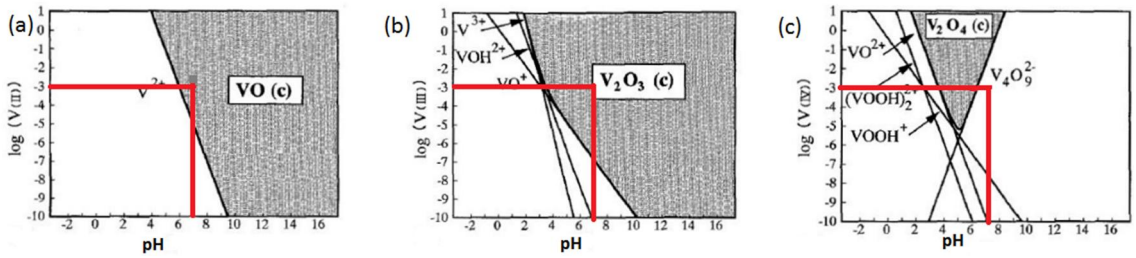

Figure 2.8 Thermodynamics of vanadium in water at 25 ℃ (a)VO,(b)V_2O_3 (c)V_2O_4, shaded area indicate existence of oxide particles, the red line is the experimental concentration found in this experiment by PLAL [123]

2.3 PLAL for Production of VO_X

Oxide stability in a solvent can be controlled by adjusting the pH of the solvent. Acids such as H_2SO_4, HNO_3 or $HClO_4$ can be used, but the presence of these acids can also initiate side reactions which will compromise the quality of the final product. One example of a side reaction using an acid is shown for H_2SO_4 in Figure 1.15. In the presence of H_2SO_4 in addition to V_2O_5 there will be products such as $[H_2VO_4]^-$, $[H_3VO_4]^-$, $[HSO_4]$, VO_2^+, $[VO_2]^+$. Characterization of such samples by Raman spectrometry will be challenging due to overlap of the peaks of the different products.

Acids in the solvent have a dual purpose, adjusting of the pH and acting as an oxidizing agent. Acids with good oxidizing properties (for example $HClO_4$) are preferable to speed up the oxidation process. However, if the acids remain in the product it will have corrosive properties during further application. Moreover, zeta potential and the stability of the particles depend on the pH. Therefore, experiments with acidic solvents have been restricted. Instead, to stabilize the oxides mixed solvents of polar protic and polar aprotic solvents have been used.

2.3.1 PLAL for Production of VO_X in DI-water-Acetone Mixtures

The solvent was prepared in such a way that the polar protic solvent acts as an oxidizer and the polar aprotic solvent acts as a stabilizer. For this purpose, water was used as a slow oxidizing agent and acetone as a good stabilizer. The solvent was prepared in the ratio of 9 % of water with 91% of acetone. That is, 3.2 ml of acetone with 0.3 ml of water was mixed using sonication for 10 min, and then transferred to quartz cuvette where the ablation of vanadium took place for 20 min. After ablation, the mixture was transferred into an air tight snap seal vial and stirred again by sonication for 10 min to disperse the nanoparticles uniformly throughout the solvent. Finally, the sample was kept for a month at room temperature.

During the one month of aging a slow reaction took place which was observed as a change of the color of the solution. In the first week the dark gray color slowly changed to light gray. In the second week it becomes colorless. In the third week it turned to slightly yellow. In the fourth week it turned to green and particles started to

precipitate. The Raman spectrum taken for a one month old sample that was dried on a steel substrate is shown in Figure 2.9.

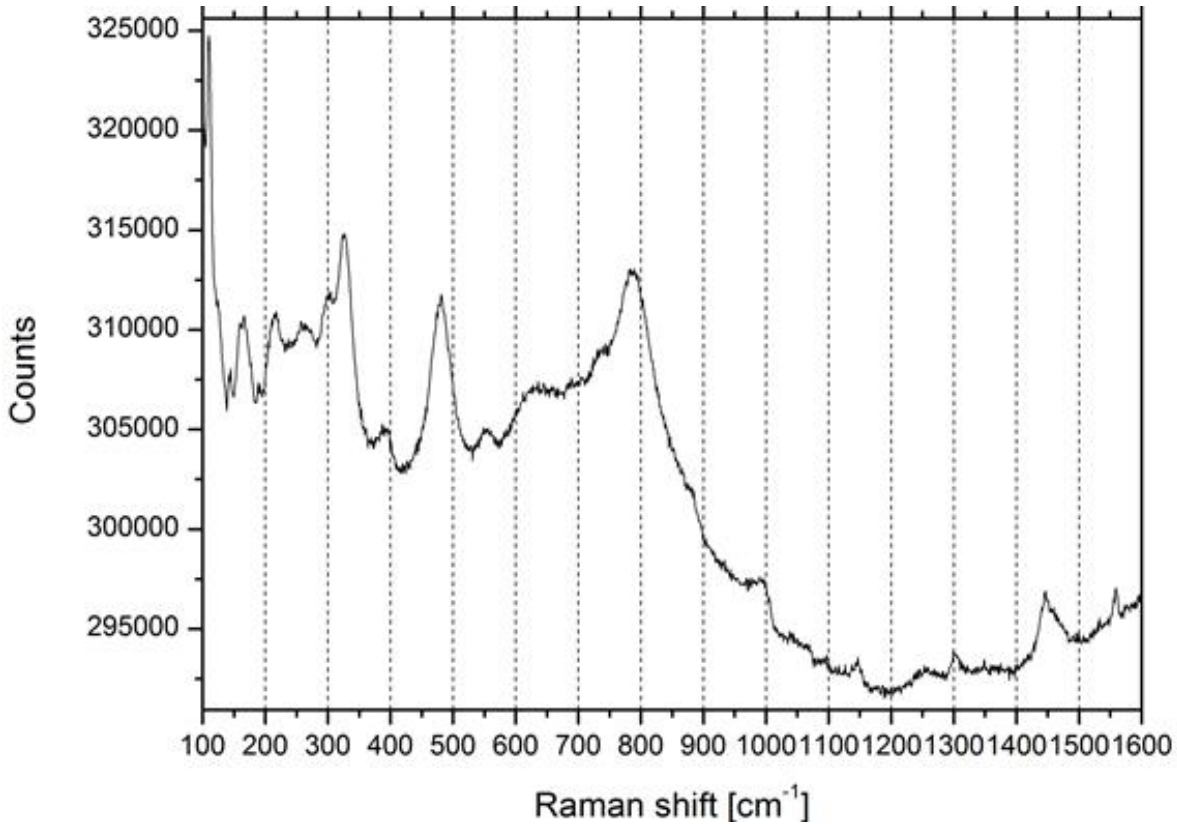

Figure 2.9 Raman spectrum of a one month old sample of VO_X prepared by ablation in 0.3ml of water and 3.2 ml of acetone

After five months the particles have kept the green color as shown in *Figure 2.10*.

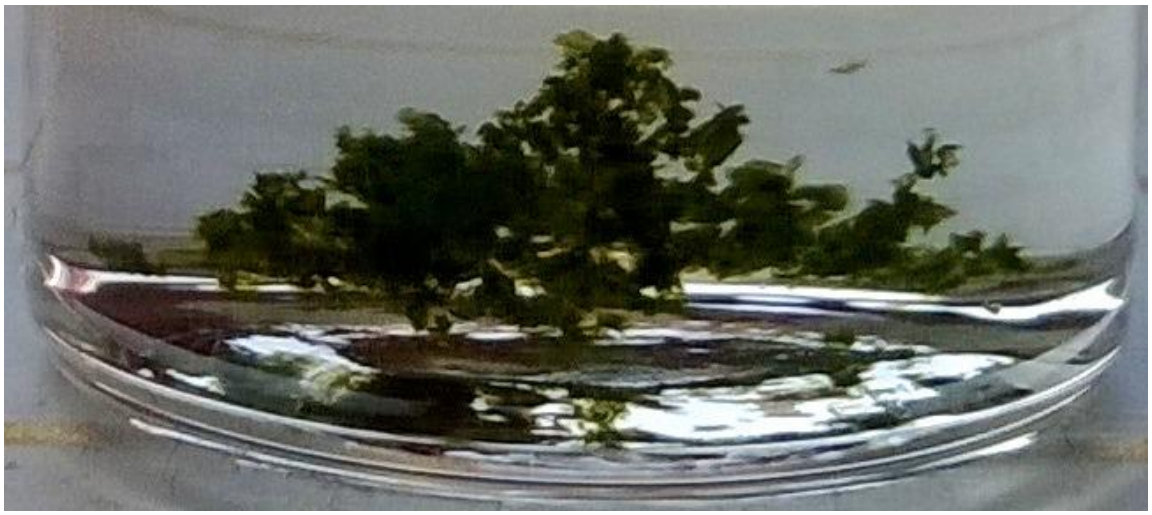

Figure 2.10 A close up photo of snap seal vial containing green precipitate in a solvent of acetone water mixture, picture taken from a five month old sample.

TEM images of the samples are shown in Figure 2.11. The precipitated particles look like narrow plates with variable dimension between 10 nm-25 nm and a length of hundreds of nanometers.

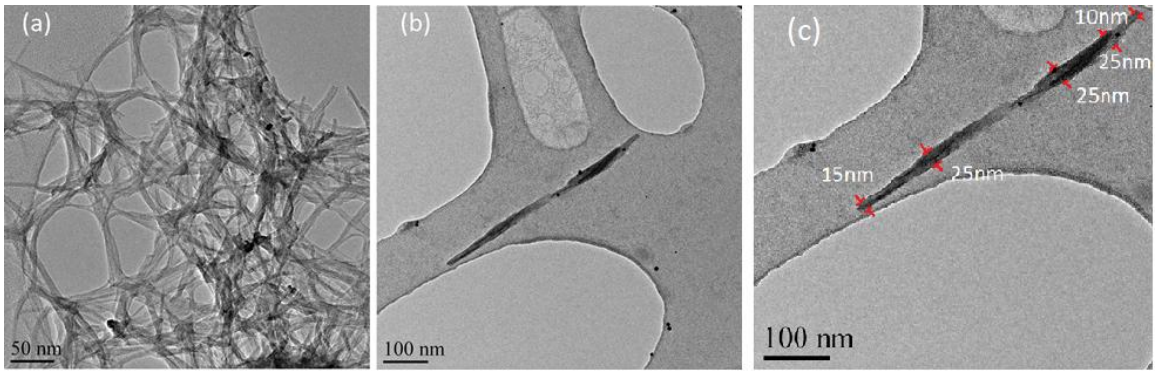

Figure 2.11 (a) TEM image of VO_X precipitated after one month (b) TEM image showing the shape of a single VO_X particle (c) TEM image of a 535 nm VO_x with variable width between 10 nm-25 nm

2.3.2 PLAL for Production of VO_X in Water-Acetonitrile Mixtures

A similar ablation experiment in a mixed solvent to control the stability of the oxide has been done. The pH of water was adjusted to 5 by addition of oxalic acid. The water solution was prepared by dissolving 0.12 g of anhydrous oxalic acid in 3.5 ml of water and the solvent was diluted until pH 5. Litmus paper has been used to measure the pH of the solution.

The solvent for ablation was prepared by mixing 3.15 ml of acetonitrile with 0.35 ml of the acidified water (pH 5). This solution was then stirred by sonication for 10min. Then, ablation was carried out for 20 min. After ablation, the solution was transferred in to a snap seal vial. Nanoparticles were dispersed throughout the solvent by sonication for 10 min. Finally, the mixture has been aged for a month.

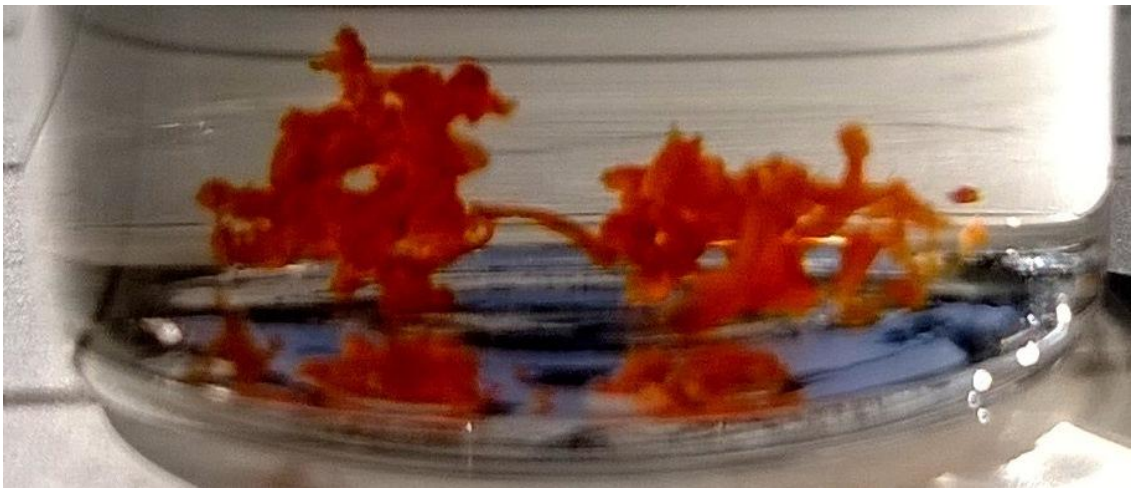

Figure 2.12 A close up photo of a snap seal vial containing orange color precipitate in a solvent of acetonitrile and acidified water at pH 5, picture taken from a 5 month old sample.

As shown in Figure 2.12, after a month the sample has produced precipitate particles with orange color. During characterization by Raman spectroscopy, laser heat transforms the particles color from orange to green. This might be due the presence of oxalic acid which is acting as reducing agent. The particles in the solvent might be in a

meta-stable state. The composition comparison between the DI-water–acetone solvent mixture and the acidified water-acetonitrile solvent mixture after laser heating has produced similar spectrum between 400 and 800 cm^{-1}as shown in Figure 2.13. At this stage of the experiment it is hard to come up with conclusive result. The experiment needs further characterization.

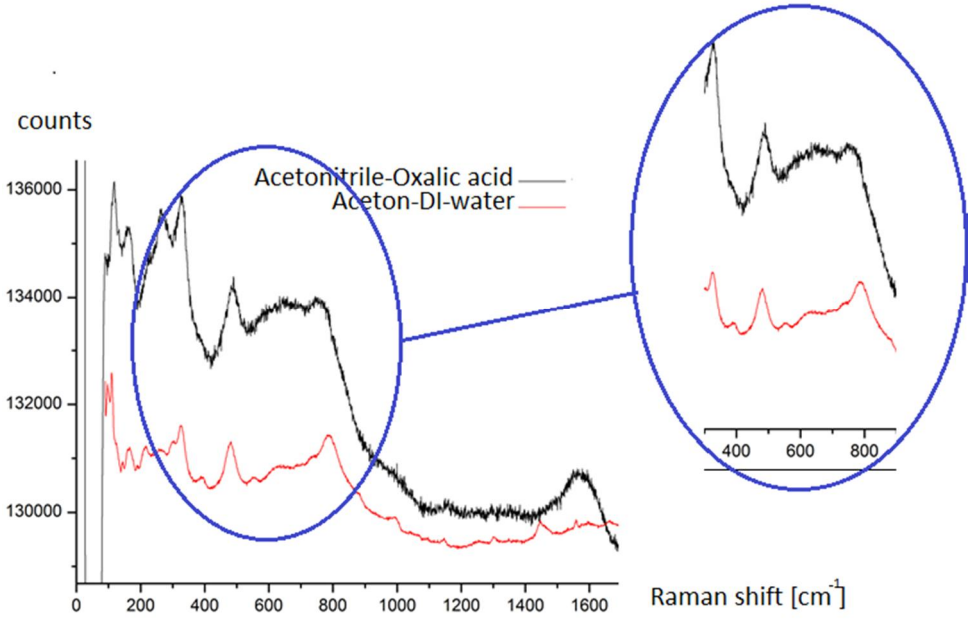

Figure 2.13 Raman spectrum comparison of acetonitrile-Oxalic acid and aceton-DI water. Despite difference in the solvent the heated particles from the acetonitrile oxalic acid solvent share some common oxide features with the acetone- DI water precipitate particles.

2.4 Reactive PLAL for Production of VO_2

As described in section 2.2.3 (PLAL for production of VO_X) the production of a stoichiometrically defined vanadium oxide is challenging by the PLAL. Production of VO_2 is particularly challenging because of its dependence on many parameters such as pH, pressure, concentration and temperature.

In this experiment production of VO_2 by a reactive PLAL in 30% hydrogen peroxide (H_2O_2) and post annealing treatment was studied. H_2O_2 is used for several reasons. First, it enables control of pH as shown in Figure 2.14. For instance, 30% H_2O_2 solution has a pH of approximately 5 which is close to the pH range where VO_2 is stable. Second, it is a good oxidizing agent. Third, it increases vanadium concentration in the solvent by etching the target. Fourth, it acts as a reducing agent in the vacuum annealing process. During decomposition of H_2O_2, H_2 will be adsorbed (intercalation) within the Xerogel ($V_2O_5.nH_2O$) due to the high affinity of vanadium for hydrogen. This adsorbed hydrogen will then act as a reducing agent in the annealing process. Fifth, the produced oxide is pure from impurities. The drawback of using H_2O_2 is it will be challenging to produce uniformly distributed nanoparticles unless a template based dep-

osition methods are used; like nanoporous silicate glass as a matrices or hydrophilic polycarbonate membrane.

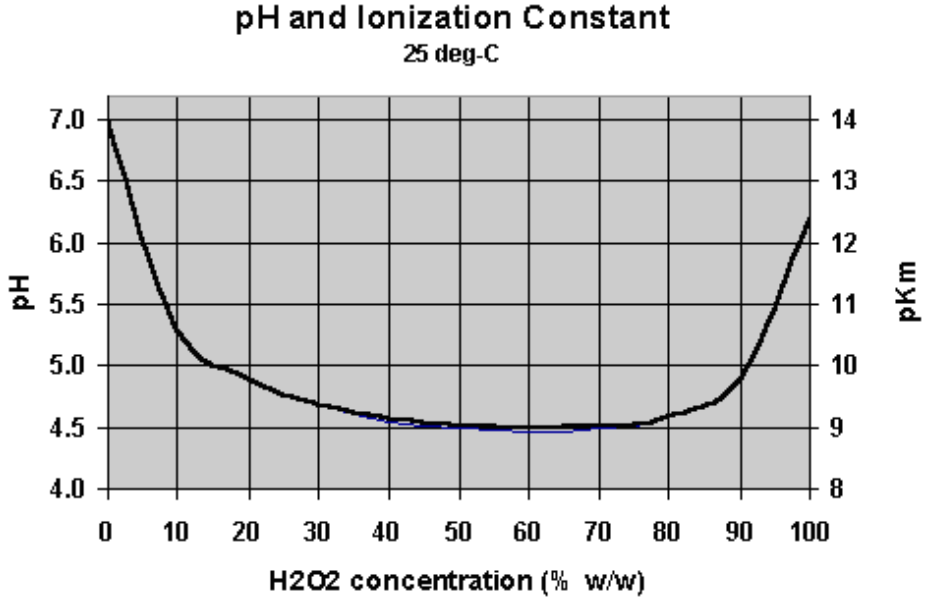

Figure 2.14 H_2O_2 pH variation based on concentration change

The experimental procedure is as follows: mass of the target was measured before and after ablation. The mass difference after ablation in 30 % of H_2O_2 is found to be 0.04389 g. 3.5 ml of 30 % H_2O_2 was measured in quartz cuvette and ablation was carried out for 20 min. During ablation because of the oxidative nature of H_2O_2 the solution turned yellow within 1-3 min. The same procedure was repeated twice to produce 7 ml of the solution. After ablation, the solutions were mixed in a 25 ml beaker. Starting at 63 ℃ the solution was heated in ultrasonic bath with a heating rate of approximately $\frac{0.12℃}{min}$ for 30 min. During the heating, the solution color changed from yellow to red within 17 min, after 10 min to muddy orange. Heating was stopped after 1 min (28 min total) with yellow solution and some brawn clusters at the bottom.

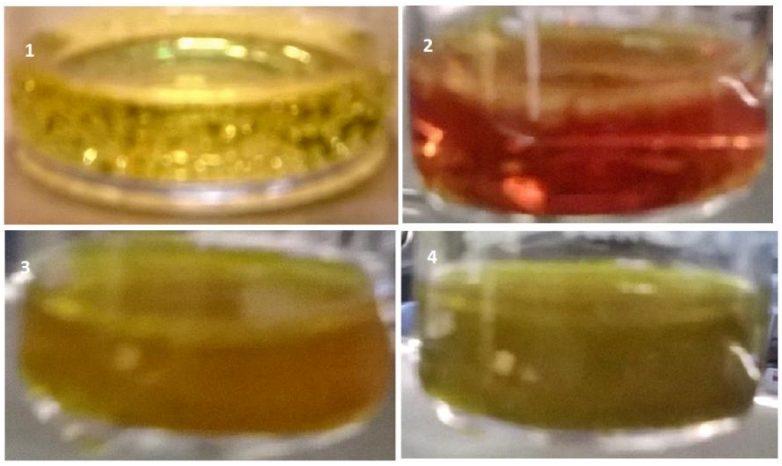

Figure 2.15 Color changes observed within 30 min during heating in ultrasonic bath 1) the initial color of the reactive PLAL product 2) color change observed after 17 min of heating 3) red color disappear within 10 min 4) heating stopped

After ultrasonic bath heating the solution was cooled to room temperature and kept in an open beaker to age for a week in to dark red gel as shown in the Figure 2.16.

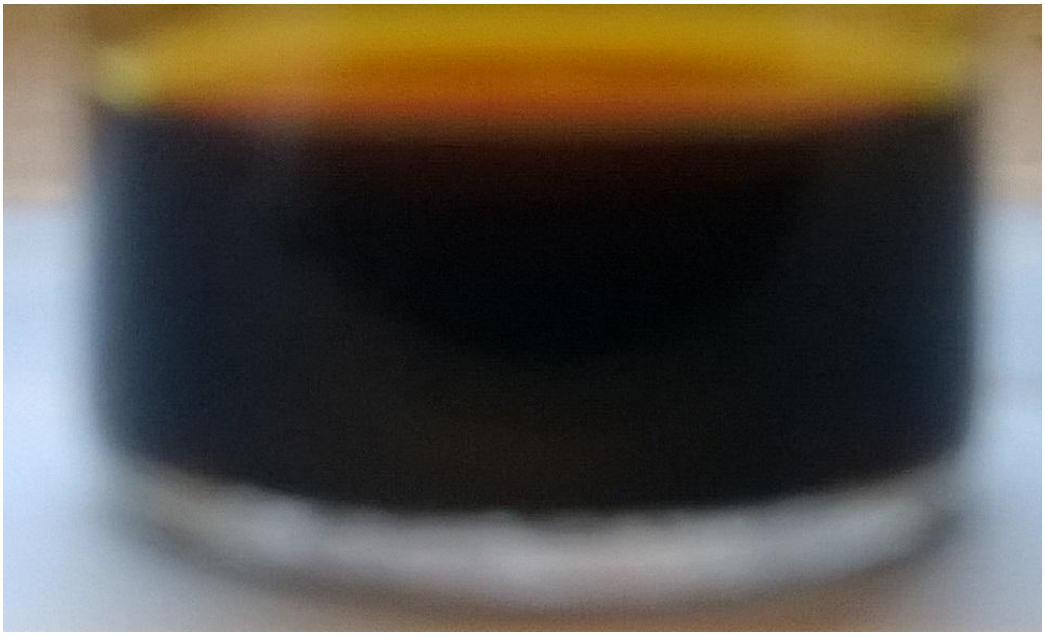

Figure 2.16 A dark red gel formed after a week of aging ($V_2O_5.nH_2O$)

The dark red gel was drop casted on a steel substrate and heated in oven at 300℃ for 1 hour to remove excess water. After cooling to room temperature in the oven, the sample was transferred to annealing in a low vacuum chamber (10^{-5} bar). The annealing was carried at 750 ℃ for 2 h with a heating rate of 20 ℃/min. After annealing, it was cooled to room temperature in the oven. As shown in Figure 2.17 the sample color changed from orange to grey.

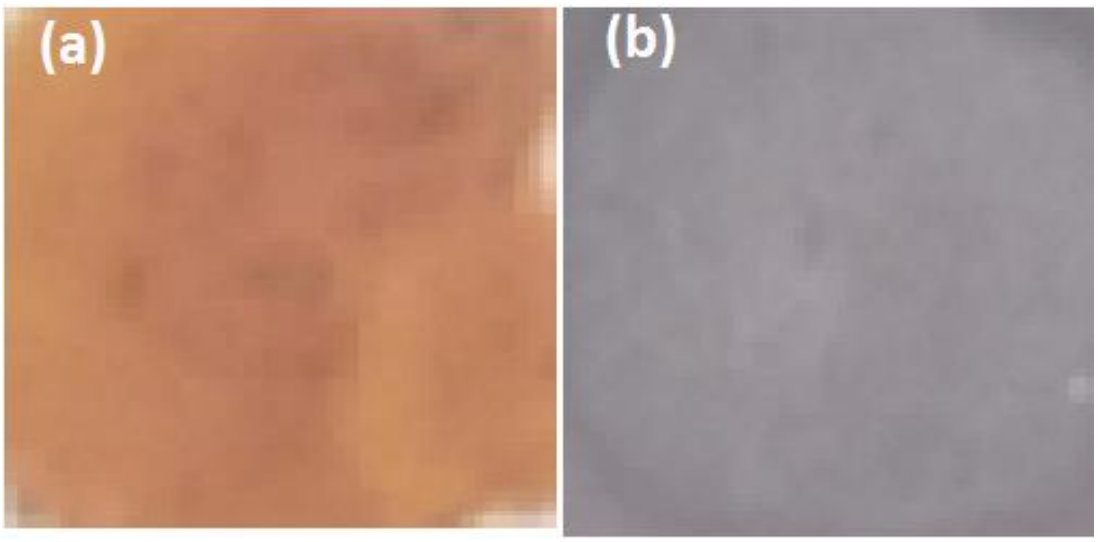

Figure 2.17 (a) photo captured from dried sample on steel substrate after drying at 300 ℃ *in air (b) after annealing in a vacuum chamber at 750* ℃

Raman spectrum was measured before and after drying at 300 ℃ reviled formation of $V_2O_5.nH_2O$. As shown in Figure 2.18, the Raman signal intensity has increased after drying due to the removal of water.

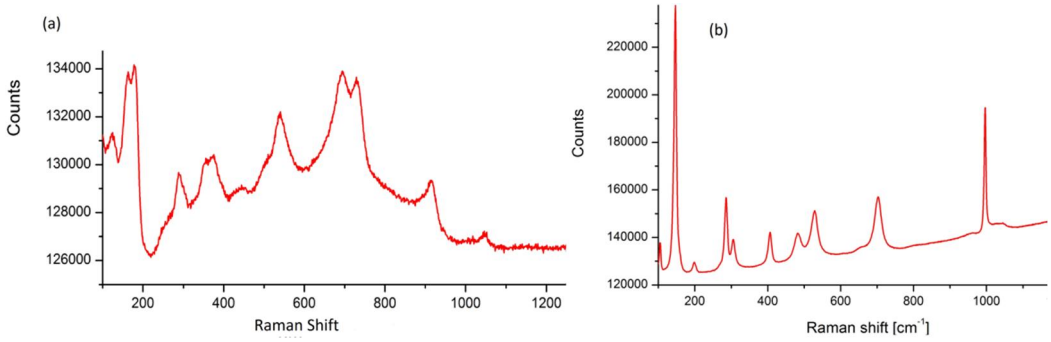

Figure 2.18(a) Raman signal from the sample before drying shows the spectrum of $V_2O_5.nH_2O$ (b) After drying at 300 ℃ the spectrum of V_2O_5

As reported by Hibino et al. [124] $V_2O_5.nH_2O$ can be synthesized by dissolving V_2O_5 in H_2O_2. The same can be achieved by dissolving V in H_2O_2 [125]. According to Alonso et al. [125] dissolution of oxides into H_2O_2 produces unstable diperoxo $[VO(O_2)_2]^-$ which then dissociate to monoperoxo $[VO(O_2)]^+$ and vanadate. After "a few hours" decavanadic acid $[H_nV_{10}O_{28}]^{(6-n)}$ is produced. The decavanadic acid slowly dissociates and undergoes polymerization to produce $V_2O_5.nH_2O$ gels. According to Fontenot et al. [126] if the ratio of H_2O_2 to Vanadium is high more of diperoxo species are formed.

In this experiment the solution turned yellow within 1 to 3 minutes of the starting of the ablation which indicates the formation of diperoxo. During heating of the sample in an ultrasonic bath the color changed to red which indicates disappearance of diperoxo. The solution slowly turned to yellow while $[VO_2]^+$ and $[H_2V_{10}O_{28}]^{4-}$ formed. During aging a condensation reaction takes place and the concentration of decavandic acid decreases and finally $V_2O_5.nH_2O$ (xerogel) is formed. The reaction path is shown in Figure 2.19, which is drawn based on the experiment comparison with theoretical references. To confirm the reaction path further Raman studies at each step is required.

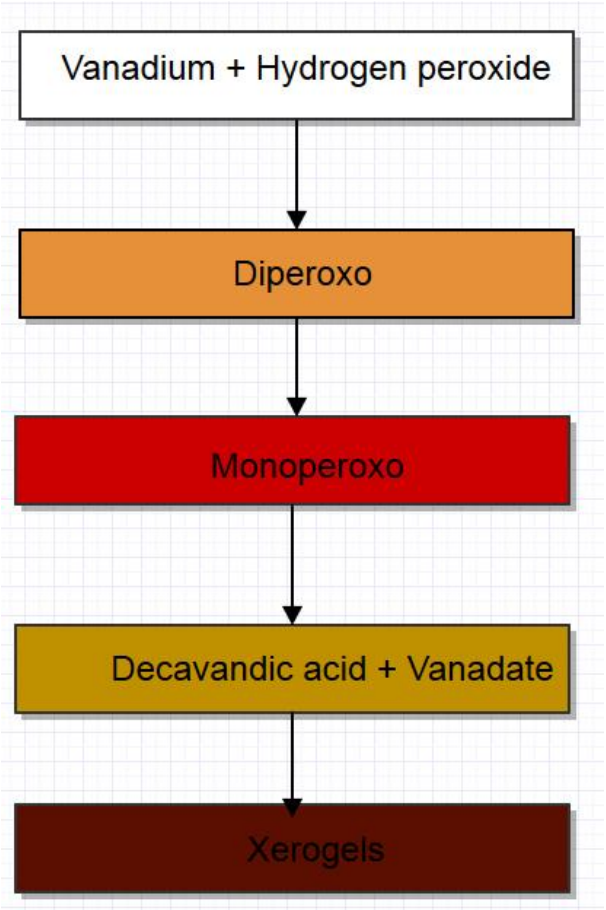

Figure 2.19 Step wise reaction during the interaction of vanadium in the presence of 30 % H_2O_2. The figure shows only the main products in each step.

A step wise reduction path also occurs during the vacuum annealing process in the order of $V_2O_5 \rightarrow V_3O_7 \rightarrow V_4O_9 \rightarrow V_6O_{13} \rightarrow VO_2$ [127]. Wang et al. reported a one-step annealing to convert $V_2O_5.nH_2O$ to VO_2. In this experiment a one-step annealing, similar to Wang et al. [83], has been used with the exception of different vacuum pressure. The annealing procedure was carried on in a low vacuum chamber (10^{-5} bar).

The formation of VO_2 and its phase transition was characterized by Raman Spectroscopy. As shown in Figure 2.20 at room temperature the Raman spectrum confirms the formation of VO_2. To check the transition from semiconductor to metallic phase the Raman spectrum was used; while the sample was heated (during the measurement). To adjust the temperature the sample was mounted on top of a heater (which works by the Peltier effect). As the temperature was increased the VO_2 changed from semiconductor to metallic phase. The phase transition is confirmed by the disappearance of the Raman signal as shown in the Figure 2.21. Cooling the sample back to room temperature was followed by reappearance of the Raman spectrum of VO_2. The experimental setup was unreliable to measure the actual temperature on the sample surface. Therefore, the exact critical temperature was not determined.

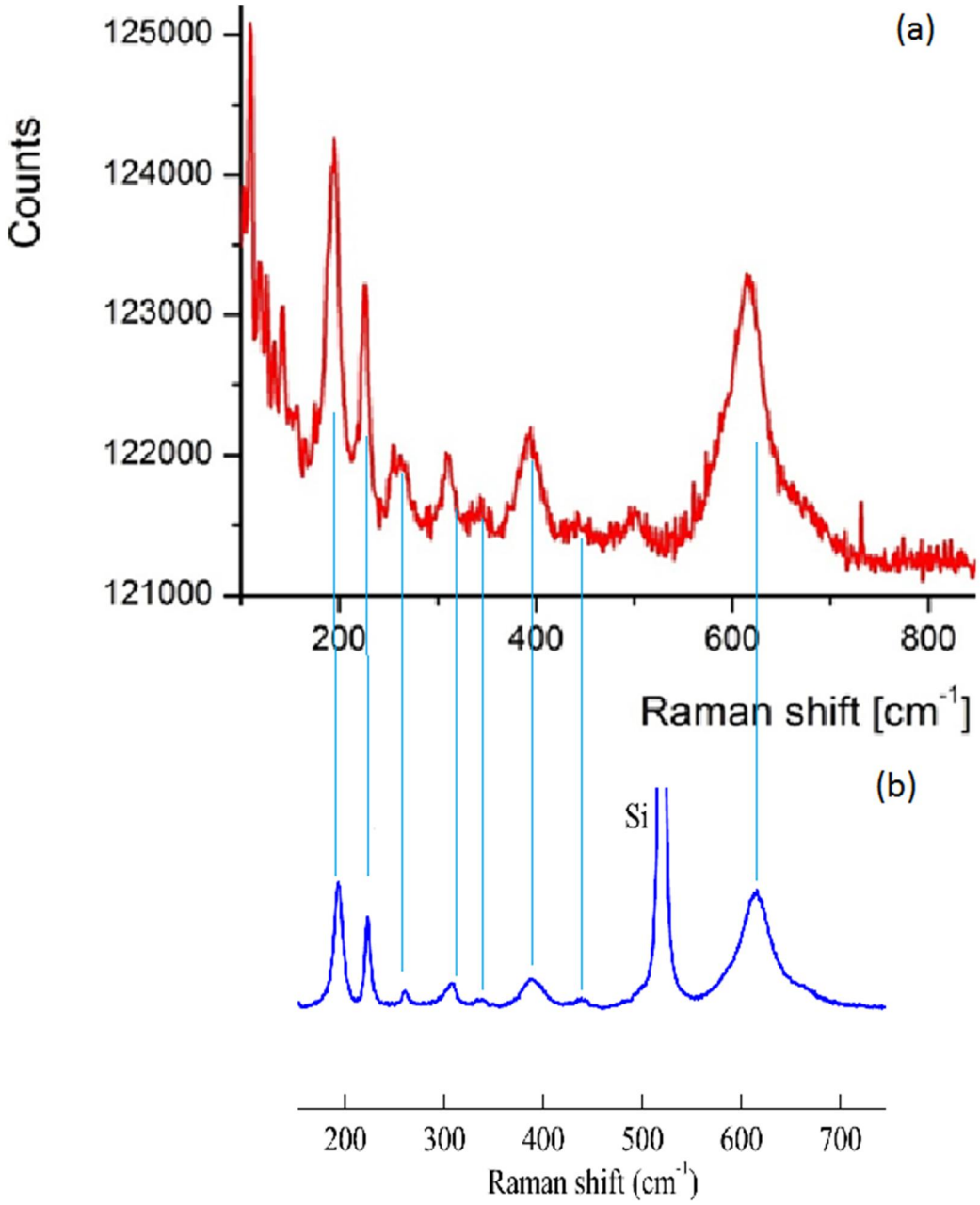

Figure 2.20(a) Raman spectroscopy of VO_2 obtained after reduction of $V_2O_5.nH_2O$ in vacuum (b) Raman reference spectrum of VO_2 copyrighted and reprinted from [128]

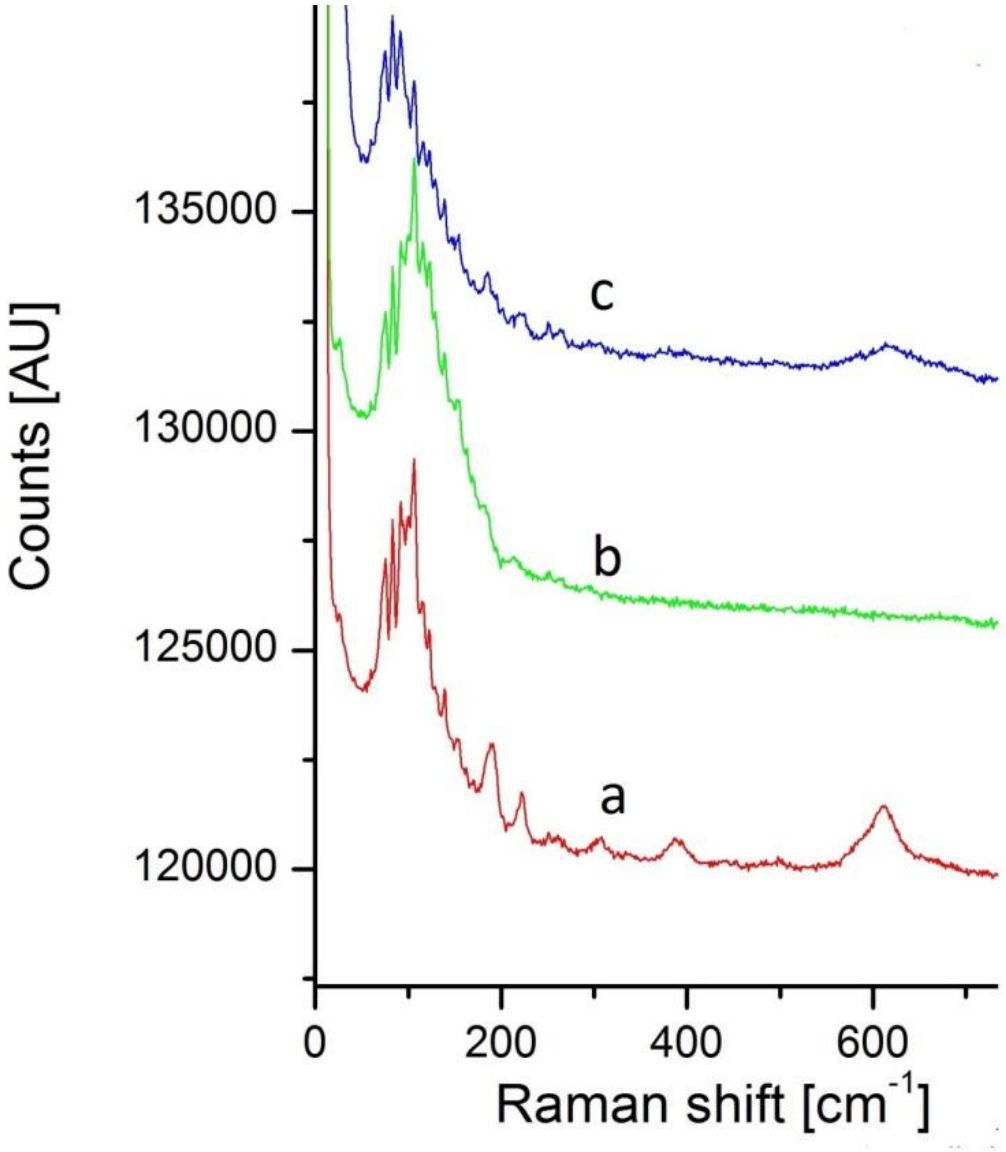

Figure 2.21 Raman spectroscopy of VO_2 measured at different temperature to confirm the existence of phase transition from semiconductor to metallic (a) Raman spectrum at room temperature (23 ℃) shows existence of VO_2 (b) at 75 ℃ the VO_2 peaks have disappeared due to the phase transition to metallic phase. (c) after cooling back to 36 ℃ the VO_2 peaks starts to reappear.

3. CONCLUSION

This thesis investigated methods to produce vanadium oxide nanoparticles by PLAL. PLAL is an environmentally friendly method for generating nanoparticles in the solvent. In PLAL airborne particles are not an issue for work safety.

In the experiment it was possible to produce VO_2, fiber like nanoparticles of VO_X and pure metallic vanadium nanoparticles. The products were characterized by SEM, TEM, optical spectroscopy and Raman spectrometry.

Due to the existence of vanadium in different oxidation states production of specific oxide require optimization of reaction conditions such as concentration, pH, temperature and pressure. In the experiment special emphasis was devoted for fabrication of VO_2 because of its near room temperature phase transition from the semiconductor to the metal phase. To produce VO_2 it was important to adjust the pH of the solution between 4 and 6 with an oxidizing acid. However, common oxidizing acids such as H_2SO_4 and HNO_3 add impurities and cause side reactions. To avoid this, great care was taken in the preparation and selection of liquid mixtures.

Production of pure VO_2 was achieved by using 30 % H_2O_2 both as an oxidizing agent and for pH control. The reaction of V with H_2O_2 leads to the formation of $V_2O_5.nH_2O$ under atmospheric pressure. To reduce $V_2O_5.nH_2O$ to VO_2 the samples were dried at 300 ℃ and then annealed at 750 ℃ for 2 hours in a vacuum chamber (10^{-5}bar). The characterization of the samples by Raman spectroscopy showed VO_2 was formed and the samples exhibit the phase transition.

Metallic vanadium nanoparticles were successfully stabilized in polar aprotic solvents (acetone, pyridine and acetonitrile). The metallic vanadium nanoparticles can be used to fabricate the desired oxides by annealing at specific temperature and pressure. This route of producing vanadium oxides offers a possible topic for future studies.

In an attempt to directly produce vanadium oxides in solutions, experiment were carried out in liquids such as acetone-water mixture and acetonitrile-acidified water mixtures; with a ratio of 9% of water as an oxidizing agent. It was possible to oxidize the metallic vanadium nanoparticles in these liquid mixtures but it was challenging to control the stoichiometry of the oxide (VO_x).

Nanoparticles produced in DI-water were found to slowly convert to VO_2^+ ions within few hours. The intermediate products were measured by Raman spectroscopy and found to be V_2O_3. Controlled production of V_2O_3 and methods of converting VO^{2+} to VO_2 are topics for future studies.

REFERENCES

[1] M. Niederberger, "Nonaqueous sol gel routes to metal oxide nanoparticles," *Americal chemical society,* vol. 40, no. 9, pp. 793-800, 2007.

[2] C. N. R. Rao , G. U. Kulkarni, P. J. Thomas, P. P. Edwards, "Size dependent Chemistry: Properties of Nanocrystals," *Chemistry a European Journal,* vol. 8, no. 1, pp. 28-35, 2002.

[3] J. Rozen, "Properties of Nanocrystalline Vanadium Dioxide", Vanderbilt University, 2005, p. 60.

[4] A. K. Brett, J. Arash, and P. Joyce, "Design of electrically driven hybrid vanadium dioxide(VO_2) Plasmonic switch," *Optics Express,* vol. 20, no. 21, pp. 23598-23609, 2012.

[5] F. A. Chudnovskii, A. L. Pergament, D. A. Schaefer, G. B Stefanovich, "Optical medium based on vanadium oxide films," *SPIE,* vol. 2777, p. 5, 1996.

[6] W. E. Case, J. L Smith, D. D. Eden, "An Examination of Vanadium Dioxide Thin Film as an Erasable/ Reusable Medium For Optical Recording," *SPIE,* vol. 0420, no. 168, p. 5, 1983.

[7] E. Strelcov, Y. Lilach, and A. Kolmakov, "Gas Sensor Based on Metal Insulator Transition in VO_2 Nanowire Thermistor," *Nano letters,* vol. 9, no. 6, pp. 2322-2326, 2009.

[8] J. Liu, Q. Li, T. Wang, D. Yu and Y. Li, "Metastable Vanadium Dioxide Nanobelts: Hydrothermal Syntesis, Electrical Transport, and Magnetic Propeties," *Angewandte Chemi,* vol. 43, no. 38, pp. 5048-5052, 2004.

[9] R. Lopez, L. A. Boatner and T. E. Haynes, "Synthesis and characterization of size controlled vanadium dioxide nanocrystals in a fused silica matrix," *Journal of Applied Physics,* vol. 92, no. 7, pp. 4031-4036, 2002.

[10] B. S.Guiton, Q. Gu, A. L.Prieto, M. S. Gudiksen, H. Park, "Single-Crystalline Vanadium Dioxide Nanowires with Rectangular Cross Sections," *Journal of the American Chemical Society,* vol. 127, no. 2, pp. 498-499, 2005.

[11] J. Nag and R. F. Haglund, "Synthesis of vanadium dioxide thin films and nanoparticles," *Journal of Physics: Condensed Matter,* vol. 20, no. 26, 2008.

[12] A. G. Bezerra, A. Barison, V. S. Oliveira, L. Foti, M. A. Krieger, R. Dhalia, I. F. T. Viana, W. H. Schreiner, "The mechanism of cysteine detection in biological media by means of vanadium oxide nanoparticles," *Journal of Nanoparticle*

Research, vol. 14, no. 1123, p. 10, 2012.

[13] A. Pyatenko, D. P. Perez, "Synthesis of silver nanoparticles with laser assistance," March 2010. [Online]. Available: http://www.intechopen.com/download/get/type/pdfs/id/9719. [Accessed 15 2 2014].

[14] H. Zeng, X. W. Du, S. C. Singh, S. A. Kulinich, S. Yang, J. He, and W. Cai, "Nanomaterials via Laser Ablation/Irradiation in Liquid: A Review," *Advance Functional Materials,* vol. 22, no. 7, p. 1333–1353, 2012.

[15] D. L. da Cunha, G. F. C Pereira, J.F.Felix, J. A. Aguiar, W. M. De Azevedo, "Nanostructured hydrocerussite compound ($Pb_3(CO_3)_2(OH)_2$) prepared by laser ablation technique in liquid environment," *Materials Research Bulletin,* vol. 49, pp. 172-175, 2014.

[16] P. P. Patil, D. M.Phase, S. A. Kulkarni, S. V. Ghaisas, S. K. Kulkarni, S. M. Kanetkar, and S. B. Ogale, "Pulsed laser induced reactive quenching at liquid solid interface: Aqueous oxidation of iron," *Physical Review Letters,* vol. 58, no. 238, 1987.

[17] D. Bonis, A. Galasso, N. Ibris, A. Santagata, R. Teghil, "Rutile microtubes assembly form nanostructures obtained by ultra-short laser ablation of titanium in liquid," *Applied Surface Science,* vol. 268, pp. 571-578, 2013.

[18] G. W. Yang, "Laser ablation in liquids: Applications in the synthesis of nanocrystals," *Progress in Materials Science,* vol. 52, no. 4, pp. 648-698, 2007.

[19] L. Yang, "Liquid phase pulsed laser ablation," in *Self-Assembly and Ordering Nanomaterials by Liquid-Phase Pulsed Laser Ablation*, Bristol, University of Bristol, 2007, p. 239.

[20] N. Takada, T. Nakano, K.Sasaki, "Formation of cavitation induced pits on target surface in liquid phase laser ablation," *Applied Physics A,* vol. 101, no. 2, pp. 255-258, 2010.

[21] K. Sasaki, N. Takada, "Liquid phase laser ablation," *Pure Applied Chemistry,* vol. 82, no. 6, pp. 1317-1327, 2010.

[22] Z. Yan, D. B. Chrisey, "Pulsed laser ablation in liquid for micro-/nanostructure generation," *Journal of Photochemistry and Photobiology C:Photochemistry Reviews,* vol. 13, no. 3, pp. 204-223, 2012.

[23] A. Kruusing, "Handbook of Liquids-Assisted Laser Processing", Amsterdam: Elsevier, 2008, p. 464.

[24] "Zeta potential analysis of nanoparticles," September 2012. [Online]. Available: http://nanocomposix.com/sites/default/files/nanoComposix%20Guidelines%20for%20Zeta%20Potential%20Analysis%20of%20Nanoparticles.pdf. [Accessed 12 10 2013].

[25] J. Liou, "Drilling contractor," 24 April 2012. [Online]. Available:

ontractor.org/refining-the-grip-on-natures-fine-grains-15705. [Accessed 15 8 2014].

[26] "Nano composix europe," New media design s.r.o, 2014. [Online]. Available: http://nanocomposix.eu/pages/characterization-techniques#zeta-potential. [Accessed 15 8 2014].

[27] "Zeta potential a complete course in 5 minutes," [Online]. Available: http://www.zeta-meter.com/5min.pdf. [Accessed 2 11 2013].

[28] F. Calvo, "Nanoalloys From Fundamentals to Emergent Applications", Lyon: Elsevier, 2013, p. 432.

[29] S. Barcikowski, A. M. Manjon, B. Chickov, M. Brikas, G. Raciukaitis, "Generation of nanoparticle colloids by picosecond and femtosecond laser ablation in liquid flow," *Applied Physics Letters*, vol. 91, no. 8, 2007.

[30] G. Yang, "Laser Ablation in Liquid: Principles and Applications in the Preparation of Nanomaterials," in *Laser Ablation in Liquid*, Singapore, Pan Stanford Publishing Pte.Ltd, 2012, p. 1192.

[31] G. A. Shafeev, "Formation of nanoparticles under laser ablation of solids in liquids," in *Laser Ablation in Liquids Principles and Applications in the preparation of Nanomaterials*, G. Yang, Ed., Moscow, Pan Stanford Publishing, 2012, pp. 327-396.

[32] M. S. Brown, C. B. Arnold, "Chapter 4, Fundamentals of Laser Material Interaction and Application to Multiscale Surface Modification," in *Laser Precision Microfabrication*, Princeton, Springer Verlag, 2010, pp. 91-120.

[33] T. Salminen, "Production of Nanomaterials by pulsed laser ablation", Tampere: Tampere University of Technology, 2013.

[34] W. M. A. Soliman, "Fundamental studies on the synthesis dynamics of nanoparticles by laser ablation in pressurized water", Nagoya: Department of electrical engineering and computer science Nagoya University, 2011.

[35] K. H. Leitz, B.Redllingshöfer, Y. Reg, A. Otto, M. Schmidt, "Metal Ablation with Short and Ultrashort Laser Pulses," *Physics Procedia*, vol. 12, pp. 230-238, 2011.

[36] V. Amendola, M. Meneghetti, "What controls the composition and the structures of nanomaterials generated by laser ablation in liquid solution," *Physical Chemistry Chemical Physics*, vol. 15, no. 9, pp. 3027-3046, 2013.

[37] T. Sasaki, Y. Shimizu, N. Koshizaki, "Preparation of metal oxide based nanomaterials using nanosecond pulsed laser ablation in liquids," *Journal of Photochemistry and Photobiology A:Chemistry*, vol. 182, no. 3, pp. 335-341, 2006.

[38] Alemu Kebede, Ashok V. Gholap, Awadhesh K. Rai, "Impact of laser energy on synthesis of iron oxide nanoparticles in liquid medium," *World Journal of Nano*

Science and Engineering, vol. 1, no. 4, pp. 89-92, 2011.

[39] K. Y. Niu, J. Yang, S. A Kulinich, J. Sun, X. W. Du, "Hollow Nanoparticles of Metal Oxides and Sulfides: Fast Preparation via Laser Ablation in Liquid," *American Chemical Society,* vol. 26, no. 22, pp. 16652-16657, 2010.

[40] J. V. A. F. J. M.Boutinguiza, "Synthesis of Titanium Oxide Nanoparticles by Ytterbium Fiber Laser Ablation," *Physics Procedia,* vol. 41, pp. 787-793, 2013.

[41] K. K. Wafaa, "Synthesis of Antimony oxide Nanoparticles by pulsed laser ablation in wet media," *Iraqi joournal of applied physics,* vol. 9, no. 3, 2013.

[42] T. Takeshi, H. Taroh,K. Tesuya, Y. Junichi, T. Masaharu, "Laser ablation of cobalt and cobalt oxides in liquids: influence," *Applied Surface Science,* vol. 243, no. 1-4, pp. 214-219, 2005.

[43] Z. Liu,Y. Yuan,S. Khan,A. Abdolvand, D. Whitehead, M. Schmidt, L. Li, "Generation of metal-oxide nanoparticles using continuous-wave fibre laser ablation in liquid," *Journal of Micromechanics and Microengineering,* vol. 19, no. 5, pp. 54008-54016, 2009.

[44] R. Rao,H. Chandrasekaran, S. Gubbalal, M. K. Sunkara, C. Daraio, S. Jin, A. M. Rao, "Synthesis of Low-Melting Metal Oxide and Sulfide Nanowires and Nanobelts," *Journal of electronic materials,* vol. 35, no. 5, pp. 944-946, 2006.

[45] P. Wagener, S. Barcikowski, N. Barsch, "Fabrication of nanoparticles and nanomaterials using laser ablation in liquids," 2011. [Online]. Available: http://particular.eu/tl_files/particular/photonik_international_2011.pdf. [Accessed 25 12 2013].

[46] T. Tsuji, Y. Tsuboi, N. Kitamura, M. Tsuji, "Microsecond resolved imaging of laser ablation at solid liquid interface: investigation of formation process of nano size metal colloids.," *Applied Surface Science,* vol. 229, no. 1-4, pp. 365-371, 2004.

[47] W. Soliman, N. Takada, N. Koshizaki, K. Saskai, "Structure and size control of ZnO nanoparticles by applying high pressure to ambient liquid in liquid-phase laser ablation," *Applied Physics A,* vol. 110, no. 4, pp. 779-783, 2013.

[48] D. J. Asunskis, "Surface Studies of Thin Films with a Focus on Potentially Protective Films on Vanadium", Manhattan, Kansas: An abstract of a Dissertation, Kansas state University, Department of Chemistry, 2005, pp. 18-20.

[49] R. R. Moskalyk, A. M Alfantazi, "Processing of Vanadium: a review," *Minerals Engineering,* vol. 16, no. 9, pp. 793-805, 2003.

[50] "Geochemical Atlas of Europe," FOREGS, 2005. [Online]. Available: http://weppi.gtk.fi/publ/foregsatlas/text/V.pdf. [Accessed 2 10 2013].

[51] G. Bauer, V. Guther, H. Hess,A. Otto, O. Roidl, H. Roller, "Vanadium and Vanadium Compounds," in *Ullmann's Encyclopedia of Industrial Chemistry*,

vol. 38, Nurnberg, Published online 15 Jun 2000 Wiley online library, 1996, pp. 49-67.

[52] N. N. Greenwood, A. Earnshaw, "Chemistry of the elements", Oxford: First published by Pergamon Press plc 1984, Second edition 1997, 1997, p. 1600.

[53] C. Röhr, "Vanadinit ore," Institut für Anorganische und Analytische Chemie, 21 4 2002. [Online]. Available: http://ruby.chemie.uni-freiburg.de/Vorlesung/Fotos/Pigmente/vanadinit.jpg. [Accessed 29 12 2013].

[54] P. S. Mitchell, "THE USE OF VANADIUM," 09 2011. [Online]. Available: http://vanitec.org/wp-content/uploads/2011/09/The-Use-of-Vanadium.pdf. [Accessed 11 9 2013].

[55] "Vanadium: A strengthening Alloy Charged With Potential," Largo Resources Ltd, 3 March 2012. [Online]. Available: http://www.visualcapitalist.com/portfolio/vanadium-a-strengthening-alloy-charged-with-potential#comment-68165. [Accessed 10 3 2014].

[56] L. Chen, C. Huang, G. Xu, L. Miao, J. Shi, J. Zhou, X. Xiao, "Synthesis of Thermochromic W doped VO_2 (M/R) Nanopowders by a simple solution Based Process," *Journal of Nanomaterials,* vol. 2012, no. 3, p. 8, 2012.

[57] "IARC Monographs on the Evaluation of Carcinogenic Risks to Humans," [Online]. Available: http://monographs.iarc.fr/ENG/Monographs/vol86/mono86-10.pdf. [Accessed 14 2 2014].

[58] Y. G. K.Takahashi, "Growth and electrochromic properties of single crystal V2O5 nanorod arrays," *Applied Physics Letters,* vol. 86, no. 5, p. 53102, 2005.

[59] A. Talledo, C. G. Granqvist, "Electrochromic vanadium pentoxide based films: Structural, electrochemical, and optical properties," *Journal of Applied Physics,* vol. 77, no. 9, p. 4655, 1995.

[60] S. S. Zumdahl, D. J. Decoste, "Chemical Principles", Florida: Mary Finch, 2009, p. 1200.

[61] M. M. Qazilbash, A. A. Schafgans, K. S. Burch, S. J. Yun, B. G. Chae, B. J. Kim, H. T. Kim, and D. N. Basov, "Electrodynamics of the vanadium oxides VO_2 AND V_2O_3," *Physical Review,* vol. 77, no. 11, p. 11, 2008.

[62] M. Eagleson, W. de Gruyter, "Concise Encyclopedia Chemistry", H. J. Hans-Dieter Jakubke, Ed., Berlin: Bibliographisches Institut and F.A.Brockhaus AG, 1994, p. 1201.

[63] J. C. Parker, U. W. Geiser, D. J. Lam, Y. Xu, W. Y. Ching, "Optical Properties of the Vanadium Oxides VO_2 AND V_2O_5," *Journal of the American Ceramic Society,* vol. 73, no. 11, pp. 3206-3208, 1990.

[64] G. Andersson, "Studies on Vanadium Oxides (I. Phase Analysis)," vol. 8, no. 9, pp. 1599-1606, 1954.

[65] C. Ban, "Synthesis and Characterization of nano scale Vanadium Oxides, Vanadium Phosphates as Cathodes for Lithium Batteries", New York: UMI Dissertations Publishing, 2008, p. 195.

[66] E. Londero, E. Schröder, "Role of van der Waals bonding in the layered oxide V_2O_5 First-principles density functional calculations," *Physical Review B,* vol. 82, no. 5, p. 8, 2010.

[67] Y. Wang, G. Cao, "Synthesis and enhanced intercalated properties of nanostructured vanadium oxides," *Chemistry of Materials,* vol. 18, no. 12, pp. 2787-2804, 2006.

[68] M. S. Whittingham, "Lithium Batteries and Cathode Materials," vol. 104, no. 10, pp. 4271-4301, 2004.

[69] V. Petkov, P. N. Trikalitis, E. S. Bozin, Simon J. L. Billinge, T. Vogt, M. G. Kanatzidis, "Structure of $V_2O_5.nH_2O$ Xerogel Solved by the Atomic Pair Distribution Function Technique," *Journal of the American Chemical Society,* vol. 124, no. 34, pp. 10157-10162, 2002.

[70] D. Vernardou, "State of the art of chemically grown vanadium pentoxide nanostructures with enhanced electrochemical properties," *Advanced Materials Letters,* vol. 4, no. 11, pp. 798-810, 2013.

[71] O. Pelletier, P. Davidson, C. Bourgaux, C. Coulon, S. Regnault and J. Livage, "A Detailed Study of the synthesis of Aqueous Vanadium Pentoxide Nematic Gels," *American Chemical Society,* vol. 16, no. 12, pp. 5295-5303, 2000.

[72] G.N.Barbosa, C.F.O.Graeff and H.P.Oliveira, "Thermal annealing effects on vanadium pentoxide xerogel films," *Eclética Química,* vol. 30, no. 2, 2005.

[73] P. Buglyó , D. C. Crans, E. M. Nagy, R. L. Lindo,L. Yang, J. J. Smee, W. Jin, L. H. Chi, M. E. Godzala Iii , G. R. Willsky., "Aqueous Chemistry of Vanadium (III) (V(III)) and the V(III)-Dipicolinate systems and a comparison of the effect of three oxidation states of vanadium compounds on Diabetic Hyperglycemia in Rats," *American Chemical Society,* vol. 44, no. 15, pp. 5416-5427, 2005.

[74] S. T. Alan, C. CDebbie, "The Chemistry of Vanadium in Aqueous and Nonaqueous Solution," in *Vanadium Compounds*, vol. 711, Colorado, American Chemical Society, 1998, pp. 2-29.

[75] J. Livage, "Hydrothermal Synthesis of Nanostructured Vanadium Oxides," *Materials,* vol. 3, no. 8, pp. 4175-4195, 2010.

[76] F. Cardarelli, "Materials Handbook", Arizona: Springer-Verlag London Limited, 2008, p. 1378.

[77] I. M. Chernenko, O. P. Mysov,O. Yu. Oleinik, A. I. Ivon, "Computer simulation of vanadium dioxide semiconductor phase formation in supersaturated solutions," *Academic Journal,* vol. 14, no. 1, pp. 51-54, 2011.

[78] U. Schwingenschlögl and, "The vanadium Magnéli phases V_nO_{2n-1}," *Annalen*

der physik, vol. 13, no. 9, pp. 475-510, 2004.

[79] P. Patnaik, "Handbook of Inorganic Chemicals", McGraw-Hill, 2002, p. 1086.

[80] J. Qi, G. Ning, Y. Lin, "Synthesis, Characterization and thermodynamic parameters of vanadium dioxide," *Materials Research Bulletin,* vol. 43, no. 8-9, pp. 2300-2307, 2008.

[81] A. I. Sidorov, O. P. Vinogradova, I. E. Obyknovennaya, T. A. Khrushehova, "Synthesis and Optical properties of Vanadium Dioxide Nanoparticles in Nanoporous Glasses," *Technical Physics Letters,* vol. 33, no. 7, pp. 581-582, 2007.

[82] S. A. Corr, M. Grossman, J. D. Furman, B. C. Melot, A. K. Cheetham, K. R. Heier, R. Seshadri, "Controlled Reduction of Vanadium Oxide Nanoscrolls: Crystal structure, Morphology and Electrical Properties," *American Chemical Society,* vol. 20, no. 20, pp. 6396-6404, 2008.

[83] N. Wang, S. Magdassi,D. Mandler, Y. Long, "Simple sol-gel process and one step annealing of vanadium dioxide thin films: Synthesis and thermochromic properties," *ScienceDirect,* vol. 534, pp. 594-598, 2013.

[84] J. J. B.Macchesney, "Preparation of vanadium dioxide". USA Patent 3,573,088, 27 July 1967.

[85] G. Li, K. Chao, H. Peng, K. Chen, Z. Zhang, "Low valent vanadium oxide nanostructures with controlled crystal structures and morphologies," *American chemical society,* vol. 46, no. 14, pp. 5787-5790, 2007.

[86] An Xin Xin, Jing Xi Ping, Jiao Huan, "Preparation of VO_2 by oxalic acid reduction method," *Chinese Journal of Inorganic Chemistry,* vol. 26, no. 7, pp. 1159-1164, 2010.

[87] L. Mao, C. Liu, "A new route for synthesizing VO_2(B) nanoribbons and 1D vanadium based nanostructures," *Materials Research Bulletin,* vol. 43, no. 6, pp. 1384-1392, 2008.

[88] L. Mao, C. Liu, "Hydrothermal synthesis of VO_2(B) nanoribbons by a mixed oxidation state precursor route," *Solid State Communications,* vol. 146, no. 9, pp. 403-405, 2008.

[89] H. Phetmung, T. W. Kim, S. J. Hwang, J. H. Choy, "A simple and direct method for synthesis of vanadium oxide ribbons like nanobelts," *Journal of the Iranian Chemical Society,* vol. 5, no. 4, pp. 706-711, 2008.

[90] F. Sediri, N. Gharbi, "Controlled hydrothermal synthesis of VO_2(B) nanobelts," *Material Letters,* vol. 63, no. 1, pp. 15-18, 2009.

[91] C. Aurelian, G. Julien, B. Pierre, O. Jean-Christophe, C. Corinne,C. Alain, "Exploiting the semiconductor-metal phase transition of VO_2 materials: a novel direction towards tunable devices and systems for RF-microwave applications," [Online]. Available:

http://www.intechopen.com/download/get/type/pdfs/id/9985. [Accessed 5 11 2013].

[92] F. J. Morin, "Oxides which show a metal to insulator transition at the neel temperature," *Physical Review Letters,* vol. 3, no. 1, pp. 34-36, 1959.

[93] B. W. Mwakikunga, E. Sideras-Haddad,M. Maaza, "First Synthesis of Vanadium dioxide by ultrasonic nebula spray pyrolysis," *Optical Materials,* vol. 29, no. 5, pp. 481-487, 2007.

[94] E. E. Chain, "Optical properties of vanadium dioxide and vanadium pentoxide," *Optical Society of America,* vol. 30, no. 19, pp. 2782-2787, 1991.

[95] J. Livage, "Optical and electrical properties of vanadium oxides synthesised from alkoxides," *Coordination Chemistry Reviews,* vol. 190, no. 192, pp. 391-403, 1999.

[96] T. D. Manning, I. P. Parkin, M. E. Pemble, D. Sheel, D. Vernardou, "Intelligent Window Coatings: Atmospheric Pressure Chemical Vapor Deposition of Tungsten Doped Vanadium Dioxide," *Chemistry of Materials,* vol. 16, no. 4, pp. 744-749, 2004.

[97] C. S. Blackman, C. Piccirillo, R. Binions, I. P. Parkin, "Atmospheric pressure chemical vapour deposition of thermochromic tungsten doped vanadium dioxide thin films for use in architectural glazing," *Thin solid films,* vol. 517, no. 16, pp. 4565-4570, 2009.

[98] T. J. Hanlon, J. A. Coath, M. A. Richardson, "Molybdenum doped vanadium dioxide coatings on glass produced by the aqueous sol-gel method," *Thin Solid Films,* vol. 436, no. 2, pp. 269-272, 2003.

[99] N. R. Mlyuka, G. A. Niklasson, C. G. Granqvist, "Mg doping of thermochromic VO_2 films enhances the optical transmittance and decreases the metal-insulator transition temperature," *Applied physics letters,* vol. 95, no. 17, pp. 171909-171912, 2009.

[100] U. D. Eugenii, "Metal Semiconductor Transition in Nanoscale Vanadium Dioxide Thin Films, Subwavelength Holes and Nanoparticles", Vols. 70-07, Tennessee: ETD Electronic theses and Dissertations, 2008, p. 198.

[101] V. Eyert, "The metal insulator transitions of VO_2: A band theoretical approach," *Wiley Online Library,* vol. 11, no. 9, pp. 650-704, 2002.

[102] S. Biermann, A. Poteryaev, A. I. Lichtenstein,A. Georges, "Dynamical Singlets and Correlation Assisted Peierls Transition in VO_2," *Physical Review Letters,* vol. 94, no. 2, pp. 26404-26408, 2005.

[103] Y. Li, S. Ji, Y. Gao, H. Luo, M. Kanehira, "Core shell VO_2 and TiO_2 Nanorods that combine thermochromic and photocatalytic properties for application as energy saving smart coatings," *Scientific Reports,* vol. 3, no. 1370, 2013.

[104] E. C. Elizabeth, "Optical properties of vanadium Dioxide and Vanadium

pentoxide thin films," *Applied Optics,* vol. 30, no. 19, pp. 2782-2787, 1991.

[105] F. Chudnovskiy, S. Luryi, B. Spivak, "Switching Device Based on First Order Metal Insulator Transition Induced by External Electric Field," *Wiley Interscience,* pp. 148-155, 2002.

[106] J. Rozen, "Properties of Nanocrystalline Vanadium Dioxide," 19 8 2005. [Online]. Available: http://sitemason.vanderbilt.edu/files/hb9eSI/qual.pdf. [Accessed 10 12 2013].

[107] P. Baum, D. S. Yang, "Highly Correlated Materials," [Online]. Available: http://thesis.library.caltech.edu/1685/7/06Chapter6-Part_II-VO_2.pdf. [Accessed 5 11 2013].

[108] J. Qi, C. Niu, "Characterization and and Thermodynamic analysis of VO_2 Synthesized by NH_4VO_3," *Energy Procedia,* vol. 17, no. Part B, pp. 1953-1959, 2012.

[109] L. Besra, M. Liu, "A Review on Fundamentals and Applications of Electrophoretic Deposition (EPD)," *Progress in Material Science,* vol. 52, no. 1, pp. 1-61, 2007.

[110] "An introduction to electron microscopy," FEI, [Online]. Available: http://www.nanolab.ucla.edu/pdf/Introduction_to_EM_booklet_July_10.pdf. [Accessed 11 12 2013].

[111] W. Zhou, R. P. Apkarian, Z. L. Wang and D. Joy, "Fundamentals of Scanning Electron Microscopy," 7 3 2013. [Online]. Available: http://home.ufam.edu.br/berti/nanomateriais/aulas%20pptx%20e%20livros/livro/Scanning%20Microscopy%20for%20Nanotechnology/Fundamentals%20of%20Scanning%20Electron%20Microscopy%20%28SEM%29.pdf. [Accessed 11 12 2013].

[112] "SEM scanning Electron Microscope A to Z Basic Knowledge for Using the SEM," [Online]. Available: http://www.teksercorp.com/docs/jeol/sem/SEM_A_To_Z_light.pdf. [Accessed 18 2 2014].

[113] C. Cayron, "IVIC instituto venezolano de investigaciones cientificas," 2000. [Online]. Available: http://cbe.ivic.ve/mic250/pdf/thesebook-chap3.pdf. [Accessed 15 12 2013].

[114] S. J. Pennycook, A. R. Lupini, M. Varela, A. Y. Borisevich, Y. Peng, M. P. Oxley, K. Van Benthem, M. F. Chisholm, "The STEM Group Materials Science and Technology Division, ORNL," 2006. [Online]. Available: http://stem.ornl.gov/papers/reviews/pdfs/Chapter6.pdf. [Accessed 15 12 2013].

[115] A. G. Mignani, L. Ciaccheri, A. A. Mencaglia, A. Cimato, "Optical Absorption Spectroscopy for quality assessment of Extra virgin olive oil", Intech, 2012.

[116] J. Z. Zhang, "Optical properties and spectroscopy of Nanomaterials", World

scientific publishing company, 2009, p. 383.

[117] J. R. Ferraro, K. Nakamoto,C. W. Brown, "Introductory Raman Spectroscopy", San Diego: Academic Press, An imprint of Elsevier Science, 2003.

[118] "Raman Spectroscopy Basics," Princeton Instruments, [Online]. Available: http://content.piacton.com/Uploads/Princeton/Documents/Library/UpdatedLibrary/Raman_Spectroscopy_Basics.pdf. [Accessed 17 12 2013].

[119] "Introduction to Raman Spectroscopy," Thermo Electron Corporation, [Online]. Available: http://www.nicoletcz.cz/userfiles/file/Aplikace/IntroductionToRaman.pdf. [Accessed 17 12 2013].

[120] P. Larkin, "Infrared and Raman Spectroscopy- Principles and Spectral Interpretation", Amsterdam: Elsevier Inc., 2011.

[121] "Raman," 2000. [Online]. Available: http://www.raman.de/htmlEN/home/advantageEn.html. [Accessed 3 1 2014].

[122] M. Miyachi, Y. Yamamoto, Y. Yamanoi, A. Minoda, S. Oshima, Y. Kobori, H. Nishihara, "Synthesis of Diazenido-Ligated Vanadium Nanoparticles," *American Chemical Society,* vol. 29, no. 17, pp. 5099-5103, 2013.

[123] G. H. Kelsall,I. Thompson,P. A. Francis, "Redox chemistry of H_2S oxidation by the British Gas Stretford process. Part IV: V-S-H_2O thermodynamics and aqueous vanadium (v) reduction in alkaline solutions," *Journal of applied electrochemistry,* vol. 23, no. 5, pp. 417-426, 1993.

[124] M. Hibino, M. Ugaji, A. Kishimoto, T. Kudo, "Preparation and lithium intercalation of a new vanadium oxide," *Solid State Ionics,* vol. 79, pp. 239-244, 1995.

[125] B. Alonso and J. Livage, "Synthesis of Vanadium Oxide Gels from Peroxovanadic Acid Solutions: A 51 V NMR Study," *Journal of Solid State Chemistry,* vol. 148, no. 1, pp. 16-19, 1999.

[126] C. J. Fontenot, J. W. Wiench, M. Pruski, G. L. Schrader, "Vanadia Gel Synthesis via Peroxovanadate Precursors. 1. In Situ Laser Raman and 51 V," *Journal of Physical Chemistry,* vol. 104, no. 49, pp. 11622-11631, 2000.

[127] Y. Ningyi, L. Jinhua, L. Chenglu, "Valence reduction process from sol-gel V_2O_5 to VO_2 thin films," *Applied Surface Science,* vol. 191, no. 1-4, pp. 176-180, 2002.

[128] Q. Yu, W. Li, J. Liang, Z. Duan, Z. Hu, J. Liu, H. Chen and J. Chu, "Oxygen pressure manipulations on the metal–insulator transition characteristics of highly (0 1 1)-oriented vanadium dioxide films grown by magnetron sputtering," *Journal of physics D:Applied physics,* vol. 46, no. 5, p. 7, 2013.

APPENDIX 1: PHASE COMPOSITION

Compostion of the samples	Temperature of preparation and quenching	Appearance of the samples	Phases observed
$VO_{1.07}$	~900°C	Dark or Medium gray powder	VO
$VO_{1.15}$	~900°C	Dark or Medium gray powder	VO
$VO_{1.20}$	~900°C	Dark or Medium gray	VO
$VO_{1.25}$	~900°C	Dark or Medium gray	$VO(+V_2O_3)$
$VO_{1.35}$	~900°C	Dark or Medium gray	$V_2O_3(+VO)$
$VO_{1.45}$	~900°C	Dark or Medium gray	$V_2O_3(+VO)$
$VO_{1.55}$	~900°C	Grayish powder	V_2O_3
$VO_{1.55}$	~900°C	Grayish powder	$V_2O_3(+VO_{1.67})$
$VO_{1.65}$	~900°C	Grayish powder	$VO_{1.67}(+V_2O_3)$
$VO_{1.67}$	~900°C	Dark gray powder or very small crystals	$VO_{1.67}$
$VO_{1.72}$	~900°C	Dark gray powder or very small crystals	$VO_{1.75}+ VO_{1.67}$
$VO_{1.75}$	~900°C	Dark lustrous powder or aggregate of very small crystals	$VO_{1.75}$
$VO_{1.77}$	~900°C	Dark lustrous powder or aggregate of very small crystals	$VO_{1.75}+ VO_{1.80}$
$VO_{1.80}$	~900°C	Nearly black lustrous powder or aggregate of small crystals	$VO_{1.80}$
$VO_{1.82}$	~900°C	Nearly black lustrous powder or aggregate of small crystals	$VO_{1.80}+VO_{1.84}$
$VO_{1.84}$	~900°C	Lustrous powder or aggregate of blue black crystals	$VO_{1.84}$
$VO_{1.86}$	~900°C	Lustrous powder or aggregate of blue black crystals	$VO_{1.84}+VO_{1.84}$
$VO_{1.88}$	~900°C	Strongly lustrous blue black powder or very small	$VO_{1.86}$
$VO_{1.92}$	~900°C	Strongly lustrous blue black powder or very small crystals	$VO_2+VO_{1.87}$
$VO_{2.00}$	~900°C	Needle or rodshaped	VO_2

		blue black crystals	
$VO_{2.15}$	≥700°C	Needle or rodshaped blue black crystals	$VO_2(+V_2O_5)$
$VO_{2.30}$	≥700°C	Needle or rodshaped blue black crystals	$V_2O_5 + VO_2$
$VO_{2.10}$	~650°C	Needle or rodshaped blue black crystals	$VO_2+V_6O_{13}$
$VO_{2.17}$	~650°C	Black lustrous powder or small crystals	V_6O_{13}
$VO_{2.25}$	~650°C	Black lustrous powder or small crystals	$V_6O_{13} +V_2O_5$
$VO_{2.50}$	~650°C	Brownish yellow powder or brownish crystals	V_2O_5